

POLITECNICO DI TORINO

DEPARTMENT OF CONTROL AND COMPUTER
ENGINEERING

Master degree course in Mechatronic Engineering

Master Degree Thesis

Optimal DC-link voltage adaptation for minimum switching losses in battery electric vehicles



Supervisor

Dr. Paolo Pescetto

Candidate

Francesca Rosa

IDNumber:278545

Academic Year 2020/2021

Table of contents

Abstract.....	10
Introduction	12
1. A-segment EV architecture	19
1.1 Traction electric motor.....	22
1.1.1 IPMSM modeling.....	24
1.2 SiC inverter	32
1.3 DC/DC converter	35
1.4 Losses in the PE converters	36
2. Control strategy	40
2.1 Motor control	41
2.1.1 IPMSM torque control regions under variable DC-link	45
2.1.2 CVC- Field Oriented Control (FOC)	50
2.1.3 Direct Flux Vector Control (DFVC)	51
2.2 Variable DC-link Control Strategy	53
2.2.1 DC/DC Control type 1	54
2.2.2 DC/DC Control type 2	55
2.2.3 DC/DC Control for 6-phase Drive	56
2.2.4 Control calibration	57
3. Simulation results	59
3.1 Simulink models	59
3.2 DC-link control for a 3-phase Drive	61
3.2.1 DC/DC control type 1	62
3.2.2 DC/DC control type 2	67
3.3 DC-link control for a 6-phase Drive	69
3.4 Inverter and DC/DC converter losses analysis	70
3.5 Experimental validation.....	74

4. Conclusions	77
References	79

List of Figures

Figure 1.1: Schematic view of the donor vehicle showing the installation of the battery in the middle of the vehicle, the DC/DC converter in the trunk and the gearbox and the motor-inverter unit at the rear axle (not to scale)[7].	19
Figure 1.2: On-board vehicle architecture.	20
Figure 1.3: FITGEN inverter-motor-transmission group (left), integration with the DC/DC converter (center) and with the project validator A-segment vehicle prototype rear axle (right) [10].	21
Figure 1.4: Main FITGEN components.....	21
Figure 1.5: Overall E-architecture and topology of the FITGEN e-axle within the vehicle. :	22
Figure 1.6: Motor performance specification (torque and power) for peak and continuous operation [10].	23
Figure 1.7: Inverter load (motor) comprising two independent three-phase systems (a), and electrical coordinate system (b) [19].	24
Figure 1.8: BPMSM d and q fluxes according to FEM analysis. (a) Flux λ_d on varying the d-axis currents, (b) Flux λ_q on varying the q-axis current.	26
Figure 1.9: Vector transformations used in the proposed controller: (a) Multiphase approach; (b) three-phase approach [19].	29
Figure 1.10: Conventional d-q reference frames ($d_1 - q_1$ for the first winding set and $d_2 - q_2$ for the second winding set) compared with the D-Q reference frames. Mutual inductance terms M_d and M_q describe the coupling between the frames in the d-q approach [18].	30
Figure 1.11: General diagram of the dual three-phase IPMSM drive architecture for a winding displacement of $2\alpha=\pi/3$: (a) conventional configuration, (b) cascaded DC-link capacitors with DC/DC converter [19].	32
Figure 1.12: Cascaded topology of the inverter used in FITGEN showing the two inverter cells and the six-phase motor connections.	33
Figure 1.13: Adopted SiC power MOSFET and its rated conduction characteristic at 175° [15].	34
Figure 1.14: Picture of BDC-546 DC/DC converter [16].	35
Figure 2.1:Block diagram of the multiphase torque control approach.....	42
Figure 2. 2: Block diagram of the VCT feedback loop [19].	43

Figure 2. 3: Block diagram of the proposed active voltage balancing algorithm.....	45
Figure 2. 4: Current circle diagram [24].....	46
Figure 2. 5: IPMSM optimal control trajectories and regions.....	48
Figure 2. 6: Torque and speed curve in DC-link voltage variation [22].	49
Figure 2. 7: Tested CVC-FOC.....	50
Figure 2. 8: Tested DFVC.	52
Figure 2. 9: Block scheme of the DC/DC control – type 1.	54
Figure 2. 10: Block scheme of the DC/DC control – type 2.	56
Figure 2. 11: Block scheme of the proposed DC-link control strategy extended to a 6- phase drive.....	57
Figure 3. 1: Model of the DC/DC converter: mask, parameters and subsystem.	60
Figure 3. 2: Model of the DC/DC control: mask, parameters and subsystem.....	61
Figure 3. 3: Simulation of the DC/DC control- light flux weakening cycle. Calibration: kDCDC =1.15; LPF cut-off frequency =30 Hz.	62
Figure 3. 4: Simulation of the DC/DC control- deep flux weakening cycle. Calibration: kDCDC=1.2, LPF cut-off frequency =30 Hz.	64
Figure 3. 5: Simulation of the DC/DC control –Response to torque reversal at 7500 rpm for kDCDC = 1.1 and LPF cut-off frequency of a) 10 Hz, b) 200 Hz.	65
Figure 3. 6: Simulation of the DC/DC control –Response to a sharp torque ramp and fast acceleration. Calibration: LPF cut-off frequency of 50 Hz and scalar gain a) kDCDC =1.1 b) kDCDC =1.2.....	66
Figure 3. 7: Simulation of the DC/DC control type 2- light flux weakening cycle. Calibration kDCDC =1.15; LPF cut-off frequency =30 Hz and kcorr = 0.6.....	68
Figure 3. 8: Simulation of the DC/DC control under sharp torque reversal at 7500 rpm (68 Km/h) without kDCDC adaptation.....	69
Figure 3. 9: Simulation of the DC/DC control type 2 combined with CVC-FOC torque control for 6-phase configuration: complex load cycle.	70
Figure 3. 10: inverter, DC/DC and total losses in the WLTP cycle with kDCDC=1.1.....	71
Figure 3. 11: inverter, DC/DC and total efficiency in the WLTP cycle with (blue) or without (red) vdc adaptation.	72
Figure 3. 12: inverter, DC/DC and total losses in the WLTP cycle with kDCDC=1.2.....	73
Figure 3. 13: inverter, DC/DC and total efficiency in the WLTP cycle with kDCDC=1.2.	73
Figure 3. 14: Experimental platform, including the motor under test and the 6-phase	

inverter [9].	75
Figure 3. 15: Experimental current and stator voltage vectors in d-q plane.....	75
Figure 3. 16: Experimental torque trajectory and DC-link voltage regulation under a speed step.....	76

List of Tables

Table 1: E-Axle Specification.	20
Table 2: Topology, winding information and performance specifications of the e-motor.	24
Table 3: Topology, semiconductor technology and target specifications of the inverter.	34
Table 4: Input and output specifications of the DC/DC converter used for FITGEN.....	35
Table 5: Inverter, DC/DC converter and total losses with $kDCDC=1.1$	72
Table 6: Inverter, DC/DC converter and total losses with $kDCDC=1.2$	74

Nomenclature

<i>Main acronyms</i>	
<i>BPMSM</i>	Buried Permanent Magnet Synchronous Motor
<i>CVC</i>	Current Vector Control
<i>DFVC</i>	Direct Flux Vector Control
<i>FW</i>	Field Weakening
<i>HSM</i>	Hybrid Synchronous Motor
<i>FOC</i>	Field Oriented Control
<i>LPF</i>	Low-Pass Filter
<i>MTPA</i>	Maximum Torque Per Ampere
<i>PI</i>	Proportional-Integral
<i>SiC</i>	Silicon Carbide
<i>SOC</i>	State of charge
<i>VCU</i>	Vehicle Control Unit
<i>EV</i>	Electric Vehicle
<i>MPD</i>	Multiphase drive
<i>PM</i>	Permanent magnet
<i>VSI</i>	Voltage Source Inverter

Abstract

Electrification is one of the macro-trends that mostly influenced research and innovation in road transportation across the last decade, aiming to provide solutions for the efficient development of EVs' components and architectures. In this context, the European founded H2020 project FITGEN (Functionally Integrated E-axle Ready for Mass Market Third GENeration Electric Vehicles) aims at designing and testing an innovative and brand-independent e-axle for the next generation of BEVs, validated on an A-segment vehicle. The developed e-axle integrates a high speed 6-phase electrical motor and *SiC* inverter, a *DC/DC* converter boosting the battery voltage to the 800 V *DC* range and a single speed transmission gearbox.

Among the other features of the FITGEN e-axle, the *DC/DC* converter permits to online adapt the inverter *DC*-link voltage for maximizing the efficiency of the power electronic converters. This thesis, developed at *Politecnico di Torino*, takes part to the FITGEN project, and in particular focuses on the evaluation of a variable *DC*-link control strategy for maximum efficiency of traction motor drive.

In order to guarantee the controllability of the traction drive in the whole speed/torque operating range and during the whole propulsion system lifetime, particular attention was devoted to the computation of the optimal set-point of the controlled electrical variables. Based on the machine model, accurate look-up table (*LUTs*) were computed to define the current and flux vector minimizing the Joule loss in the entire operating range. This includes MTPA tracking and FW operation, both under variable *DC*-link. Dealing with the *DC/DC* converter, the computed *LUTs* also permit to define the optimal *DC*-link voltage on varying the motor torque and speed. At first, based on the computed *LUTs*, the torque and the optimal *DC*-link voltage references were directly imposed, and the system response was tested in the simulation platform. Anyway, since the *LUTs* are computed based on the motor model, accurate knowledge of its parameters, and particularly the magnetic saturation characteristic, is necessary. Therefore, two control strategies, namely “**Control type 1**” and “**Control type 2**”, were analyzed for automatically adapting the *DC*-link voltage to minimize the losses in the inverter and in the *DC/DC*. Particular effort was devoted to the optimal calibration procedure, requiring a tradeoff between fast motor control dynamic with reliable safety margin and power loss minimization at medium speed.

Additionally, the calibration procedure needs to consider the relevant actuation delay of the DC/DC converter.

One of the key features of these two solutions is that the optimal DC -link adaptation is almost independent by the adopted motor control strategy. To prove this assert, the global system, including the drive and the DC/DC , was tested in the Matlab-Simulink environment with two motor control algorithms, namely $CVC - FOC$ and $DFVC$. Despite the reference FITGEN drive is a 6-phase system, the DC/DC control was initially tested for an equivalent 3-phase motor for debugging and calibration purposes, simulating the two three-phase sets connected in parallel. Then, the DC/DC control has been extended to the 6-phase case. Moreover, to confirm the expected performance of the proposed control strategy, the obtained aggregate losses reduction (DC/DC converter + inverter) was numerically evaluated based on a loss analysis of the two converters.

Introduction

Today's economy has to face the challenge of finding solutions to megatrends like the connectivity, mobility and growing ecologic thinking. From a present-day perspective, electrification of road transport seems to be a key challenge to achieve the emission targets while enabling efficient mobility for people and goods. Indeed, nowadays the large dependency of the present energy consumption from imported fossil fuels and the soaring oil prices push the research for alternative solutions respect to the traditional people transportation system, including road vehicles [1].

About 80% of the worldwide CO_2 emissions stem from large cities and their metropolitan areas. The sector of transports alone in the worldwide emissions covers about 20% [1]. With the growing urbanization and the creation of so-called mega-cities new requirements on the old automobile paradigm are required. Pollution, noise and traffic congestion are an ever-growing problem in the bustling metropolises. Under this scenario, electric mobility is considered as a promising option for future individual transportation to contribute to energy diversification and greenhouse gas emissions reduction objectives. Indeed, with respect to the internal combustion engine vehicles, electric vehicle benefits include zero tailpipe emission, better efficiency and large potential for greenhouse gas emissions reductions when coupled with a low-carbon electricity sector [2]. Thus, with the technological development, the natural bet is a revolution in the transportation sector aiming the electric mobility. This could be obtained implementing alternatives to the vehicles with Internal Combustion Engines (ICE), such as Battery Electric Vehicles (BEVs).

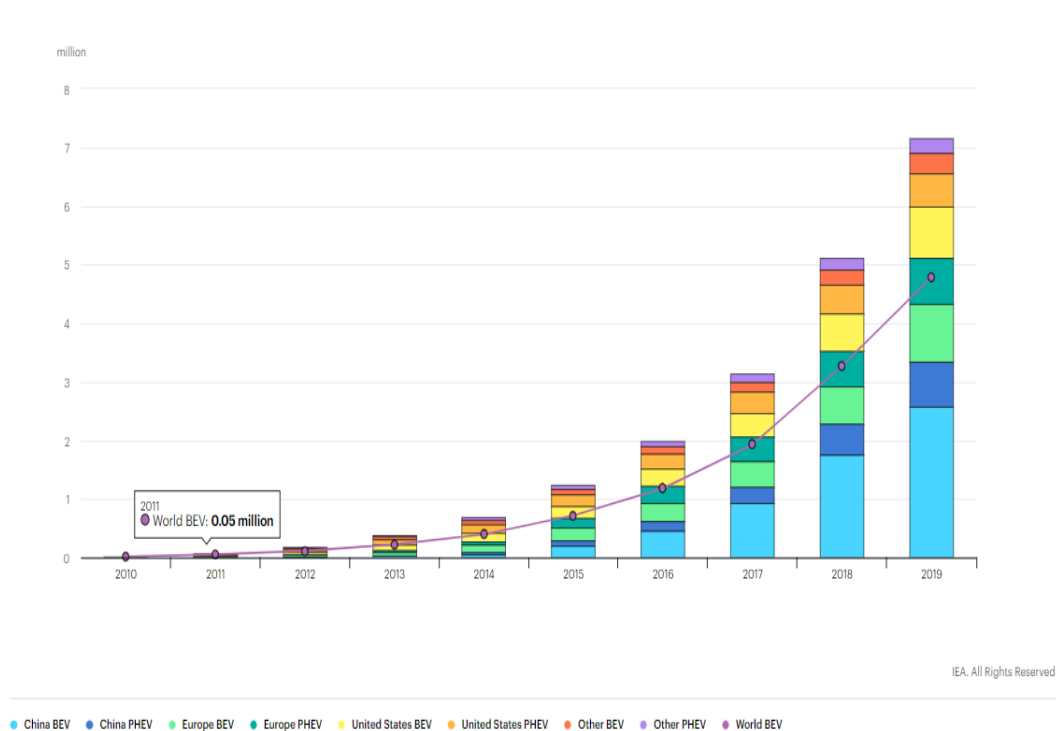
These objectives are major drivers behind countries' policy support in the development and deployment of electric powertrains for transport. Indeed, in recent years, ambitious policy announcements have been fundamental in stimulating the electric-vehicle rollout in major vehicle markets. The continuous policy approaches that rely more on regulatory and other structural measures – including zero-emission vehicles mandates and fuel economy standards – have set clear, long-term signals to the auto industry and consumers to support this significant transformation in the automotive sector. Therefore, there is a strong political commitment worldwide towards green mobility and reduction of pollutant emissions, with the aim of tackling the issue of climate change and the air quality, especially in large urban areas. The expected results are addressing to face this urgency through the reduction of the emissions at the source level. To date, 17 countries have

announced 100% zero-emission vehicle targets or the phase-out of internal combustion engine vehicles through 2050 [2][3].

Thus, the automotive industry is undergoing a significant transformation with the arrival of new types of vehicles, services, requirements and uses that break away from the traditional model of cars. The very nature of mobility is changing. User behavior is shifting as well as consumers aspiration attached to private cars, which expect performance improvements at no additional costs. In today's electric car market, the consumer profile is evolving from early adopters and technophile purchasers to mass adoption. Therefore, to reduce the risk of potential failures and to significantly reduce the production costs, a profound maturity in terms of technological development is required. The need for the technology to mature is also ensuring a smooth transition from the user perspective, in terms of driving performance and cost. The customer demands (e.g. higher performance levels, drivability and comfort, improved safety and styling) must be met at acceptable costs (purchase costs as well as the operating costs despite the trend of rising fuel prices)[3].

A look back at the history of the automobile reveals not only how our relationship to the car object is altering, but also the need for a different approach to the current concept of mobility. New services (self-service cars, car-sharing, carpooling) are making a significant contribution to the emergence of a new ecosystem. The consequent industrial, economic and ecological situation involves all of the traditional protagonists in the sector, i.e., car and parts manufacturers, recyclers, energy and fuel suppliers, as well as market newcomers like engineering, computing and communications companies.

Therefore, today's global automotive industry is at the cusp of a paradigm shift from internal combustion engine vehicles to zero emission vehicles. In this regard, Electric Vehicles (EVs) have obtained an unprecedented significant interest in recent times, emerging as the one of the most promising alternative powertrain technologies with zero tailpipe emissions and long-term economic viability [4]. The global electric vehicle fleet expanded significantly over the last decade, underpinned, as has been already said, by supportive policies and technology advances. The market for electric and hybrid vehicles has begun to exploit its potential and sales of electric cars topped 2.1 million globally in 2019, surpassing 2018 – already a record year – to boost the stock to 7.2 million electric cars, with the largest share in China (45%) and 25% equal shares in Europe and US, as reported in *The Global EV Outlook* publication [2].



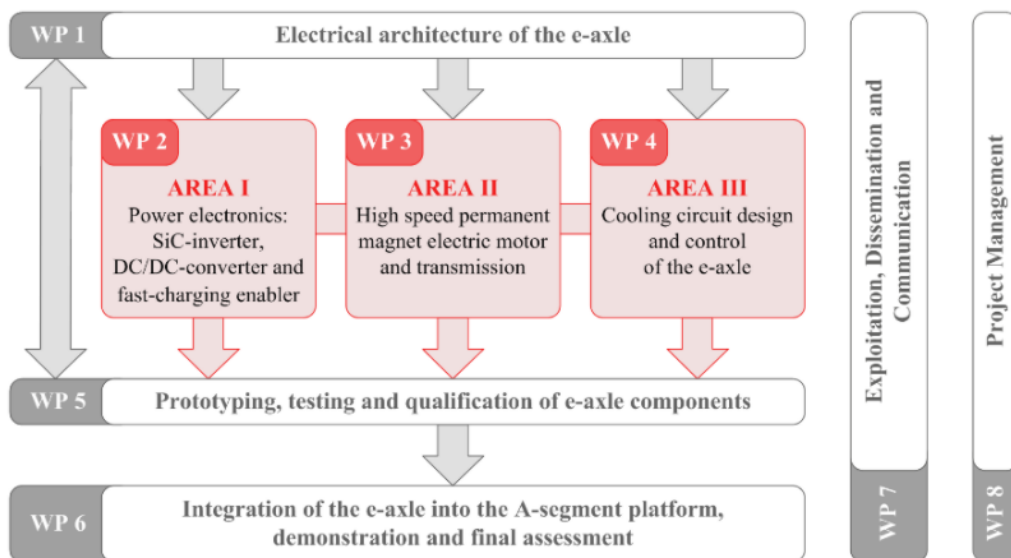
Global electric car stock 2010-2019 [2]

Recent figures suggest a xEV market share of 6% by 2020, 24% by 2025 and 48% by 2030 with 24 million vehicles per year expected to be sold by 2030 and a global market turnover of greater than 700 billion EUR per year, including 50 billion EUR due to electrified powertrain [2].

Electrification is therefore the macrotrend that has most influenced research and development activities in road transportation across the last decade. Main challenges for large scale deployment include higher maturity with respect to performance, development efficiency or production costs. Significant private and public investment have been made to tackle these challenges and business opportunities, aiming to provide solutions for the efficient development and validation of electrified vehicles, as well as for the advance in innovative architectures, components and systems for next generation electrified vehicles. In in this context, the European H2020 FITGEN aims to develop a functionally integrated e-axle to be validated in an A-segment vehicle validator. FITGEN proposes technical advancements under each element of the electric powertrain, featuring a 6-phase Buried-Permanent-Magnet Synchronous Machine, driven by a SiC-inverter and coupled with a high-speed transmission. It is complemented by a DC/DC-converter for high voltage operation of the motor in traction and for enabling super-fast charging of the 40 kWh battery (120 kW-peak) plus an integrated AC/DC on-board charger.

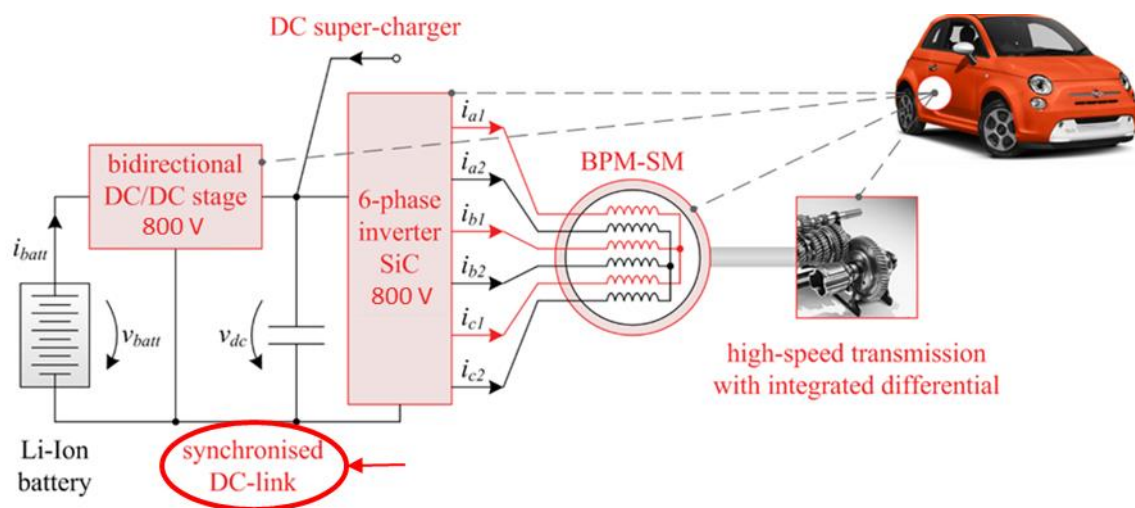
The FITGEN project, started in early 2019, aims to improve the existing EVs technology respect to the 2018 state of the art. The development is split into three main areas [6]:

- **Area 1** “*power electronics and charger*”, which comprises the *DC/DC* converter and the SiC-drive inverter. The aim is to increase the power density by 50% thanks to the adoption of the SiC power MOSFET components, targeting a peak efficiency of 99% and ensuring embedded charging and super-fast charging capability.
- **Area 2** “*electric motor and transmission*”, which includes the high-speed electric motor and the corresponding gear box. The gravimetric power density will be increased by 40% thanks to a high-speed Buried Permanent Magnet-Synchronous Machine (BPMSM), with operation up to 20,000 *rpm* and peak efficiency at 96.5%;
- **Area 3** “*cooling and control*”, which includes all the cooling and control topics of FITGEN. Several solutions of cooling system are investigated, including a strongly optimized liquid cooling system for the machine and converters functionally integrated with the oil cooling system required for the transmission gearbox. Moreover, an optimized control of the SiC inverter and the *DC/DC* converter is developed, enabling e-motor high-voltage operation during traction mode.



Subdivision of the FITGEN structure into the main areas of interest [8].

The following figure [5] shows a schematic of the architecture of the FITGEN e-axis, including the main components and a simplified electrical scheme.



Layout of the high voltage powertrain system

In particular, the treated case of study is part of the FITGEN Area 3 and proposes an optimized control strategy for online adapting the DC -link voltage in a traction motor drive, for minimizing the aggregate losses (DC/DC and inverter), without limiting the DC/DC motor control dynamic capabilities. The developed DC/DC control strategy, combined with the motor control algorithm developed by Tecnalía (*Fundación Tecnalía Research & Innovation*) institute, one of the FITGEN consortium partners, permits high performance and high total efficiency of the e-Axle, with minimum power losses.

The target of this work is defining an optimal voltage reference for the DC/DC converter between the battery and the traction inverter, which boosts the battery voltage (rated 400 V) to a controlled DC -link, which feeds the traction inverter. The amplitude of the DC -link is online varied depending on the drive operating conditions in order to minimize the power losses in the DC/DC converter and in the traction inverter, without limiting the motor control dynamic performance.

In the first chapter, the A-segment EV architecture is presented and a literature review on the main components is covered. First, MPDs, which are suitable solutions in EV applications, are presented. Among these, dual three-phase interior permanent magnet synchronous machine drive, which characterize the FITGEN e-axle, has been considered. Then, an overview on the SiC inverter and the DC/DC converter components, with their electric specifications and requirements, are covered. The FITGEN SiC inverter is a hard switching, six-phase inverter, using SiC power MOSFETs. The DC/DC , instead, is a commercial product [16] and is used to boost the battery voltage to the DC -link voltage of the inverter and to allow for high power charging. Moreover, the chapter addresses a loss

analysis of the traction inverter and the DC/DC converter.

The second chapter focuses on different control system developments for the motor-inverter, under variable DC -link. In particular, the CVC-FOC and the DFVC are being introduced, considering first an equivalent 3-phase motor supplied by half of the DC -link, and then the 6-phase drive configuration. Moreover, it includes an overview of the IPMSM torque control regions. To this purpose, based on the machine model, accurate look-up table ($LUTs$) were computed to define the current and flux vector minimizing the Joule losses in the entire operating range. This includes MTPA tracking and FW operation, both under variable DC -link. This chapter aims also to examine the DC -link optimal adaptation control. A key advantage of the proposed algorithm is that the motor control and the DC/DC converter are treated as independent black boxes, so it is applicable whatever the adopted DC/DC converter structure and torque control strategy. In turn, the proposed DC/DC control can be considered suitable for a wide range of drive applications. In particular, two strategies, “**Control type 1**” and “**Control type 2**”, were developed for automatically online adapting the DC -link voltage independently by the motor parameters. Control type 1 is simpler to implement and calibrate (it requires only two calibration parameters), providing a good dynamic performance overall but the DC -link voltage is not deeply optimized. Control type 2, instead, further optimizes the DC -link voltage control at the cost of more complicated calibration procedure. Lastly, a control calibration procedure is also covered.

The third chapter focuses on the e-motor components modelling and provides an analysis of the results coming from tests validated in Matlab-Simulink environment. The DC/DC control was tested when combined with two motor control strategies, namely CVC – FOC and DFVC. For each case, the DC/DC control was tested for the equivalent three-phase motor drive first, considering the two three-phase sets of the reference machine connected in parallel. Then, the DC/DC control has been extended to the six-phase case. Moreover, based on the computed $LUTs$, the torque and the optimal DC -link voltage references were directly imposed, and the system response was tested in the simulation platform. A numerical evaluation of the aggregate losses reduction (DC/DC converter + inverter) based on a loss analysis of the two converters is also covered.

Lastly, the fourth chapter focuses on the experimental validation, carried out by Tecnalia partner in their facilities, while chapter five summarizes the conclusions and final considerations.

CHAPTER 1

1. A-segment EV architecture

The e-axle proposed by the FITGEN project is based on a reference platform (A-segment vehicle) and features a DC/DC converter, a motor-inverter unit and a gearbox, c.f. Figure 1.1. The donor vehicle is a FIAT 500-electric [7].

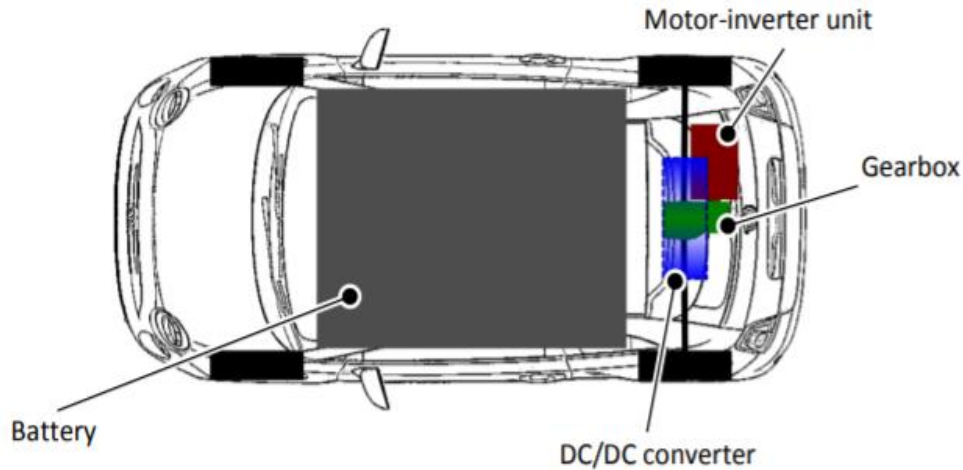


Figure 1.1: Schematic view of the donor vehicle showing the installation of the battery in the middle of the vehicle, the DC/DC converter in the trunk and the gearbox and the motor-inverter unit at the rear axle (not to scale)[7].

In particular, the on-board vehicle architecture is shown in Figure 1.2 [8], while its main specifications are given in Table 1. The considered e-axle includes a latest generation Buried-Permanent-Magnet Synchronous Machine (PMSM), driven by a SiC-inverter and coupled with a high-speed transmission. It is complemented by a bidirectional DC/DC -converter for high voltage operation, elevating the battery voltage v_b from a rated 400 V to a controlled v_{dc} up to 750 V, which feeds the six-phase inverter and ultimately the dual three-phase PMSM. This allows for high power fast charging operation. A DC/DC controller is implemented in the overall control design for maximizing the system conversion efficiency, i.e., for minimizing the power losses in both the traction inverter and the DC/DC converter. This is obtained by online minimizing the DC -link voltage v_{dc} without limiting the torque control performance. To this purpose, optimal current and DC -link voltage set-points computation is required, to guarantee efficient operation of the traction drive even under variable DC -link voltage, including MTPA and field weakening (FW) range. The DC/DC converter is described in section 1.3, whereas its control strategy is covered in chapter 2.

Furthermore, a six-phase motor design, consisting of two three-phase systems, is used. The motor-inverter unit is described in sections 1.1 and 1.2. The high-speed transmission includes a gearbox connecting the motor and the drive shafts to the wheel and is implemented in a separated housing with respect to the one of the motor-inverter.

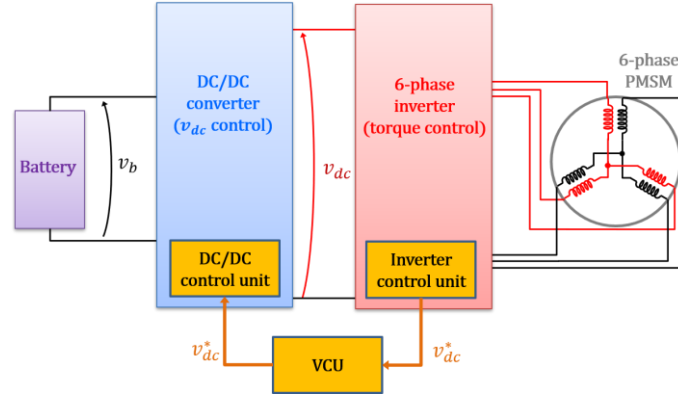


Figure 1.2: On-board vehicle architecture.

<i>E-AXLE SPECIFICATIONS</i>	
Battery voltage	320÷420 V
Max v_{dc}	750 V
Max continuous power	180 kW
Continuous torque	80 Nm
Peak torque	170 Nm
Peak power	135 kW
Max speed	22500 rpm
Base speed at max T	8000 rpm

Table 1: E-Axle Specification.

Figure 1.3 depicts the results of the installation configuration. The group inverter-motor-transmission is integrated as a mono-block (left), on top of which the DC/DC is installed on a supporting frame (centre), minimising the cable length. Then, the proposed e-axle is mounted in rear wheel driving configuration (right) in the vehicle prototype chassis, using the space in the trunk and applying a mechanical modification to the rear suspension

system. With respect to the requirements of the demonstrator A-segment full electric vehicle platform, the adopted configuration provides the best tradeoff between reduced complexity of the setup, geometric compatibility of the components and frame, and overall performance of the e-axle [10].

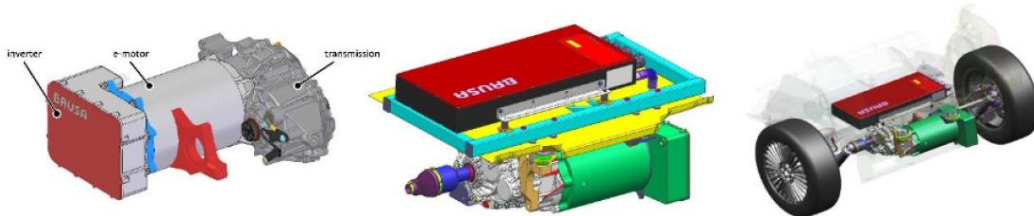


Figure 1.3: FITGEN inverter-motor-transmission group (left), integration with the DC/DC converter (center) and with the project validator A-segment vehicle prototype rear axle (right) [10].

The three main components, i.e., the inverter, the integrated permanent magnet motor and the gearbox with differential, are integrated into one physical unit as shown in Figure 1.4 [11]. The motor torque control and the variable DC -link control algorithms are executed into the MicroAutoBox controller board, connected via a multicore cable to the inverter board.

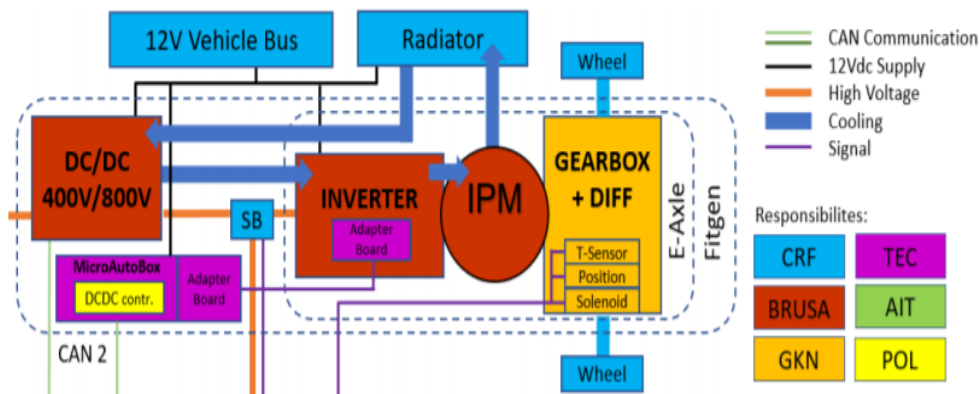


Figure 1.4: Main FITGEN components.

All active components are also connected to the $12 V_{dc}$ net for power supply, which is depicted by black lines. As can be noticed from Figure 1.5 [11], no direct communication between the inverter control unit and the DC/DC converter is allowed. The reference voltage v_{dc}^* command is communicated from the MicroAutoBox to the Vehicle Control Unit (VCU) and then from the VCU to the DC/DC via CAN protocol. [11].

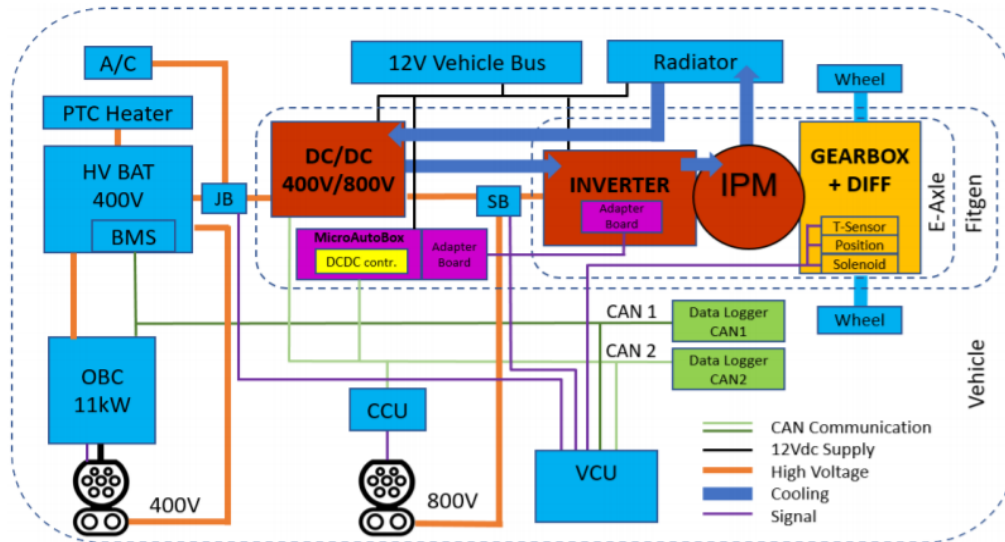


Figure 1.5: Overall E-architecture and topology of the FITGEN e-axle within the vehicle.

The requirements and the modeling of the relevant components of the system to be controlled, i.e. the electric motor, the inverter and the DC/DC converter, are presented in the following section. Therefore, at first, the characteristics of the electric motor are described. Then, the specifications defined for the inverter are outlined. Finally, the requirements for the control of the DC -link are displayed.

1.1 Traction electric motor

In recent decades, thanks to their distinctive features, i.e. power splitting, lower torque pulsations and fault tolerance, that provide notable performance improvements compared with their conventional three-phase counterparts, MPDs have achieved a such great success to be considered suitable candidates for replacing three-phase drives in Electric Vehicle applications [13].

Among multi-phase drives advantages, it should be highlighted the following ones:

- Compared to three-phase motors, the same power can be achieved by lower phases current, which makes it possible to use low voltage or low current inverters;
- Some low order space harmonics can be eliminated in multi-phase motor drives, so the torque propulsion can be highly reduced;
- The current harmonics to DC -link capacitor of multi-phase inverter can be reduced, depending on the motor control strategy used;
- The reliability of system can be significantly improved, i.e., when one or several

phases are at fault, multi-phase system can keep running at lower load.

In particular, among multiphase solutions, dual three-phase Permanent Magnet Synchronous Machine PMSM has attracted great attention in various industrial applications, particularly in propulsion systems for EVs, and it is what has been selected for the FITGEN project. The attractiveness is due to the high-power density, high efficiency, wide speed range, fast torque-speed response, and the relatively decreasing price of PM materials. Indeed, the permanent magnet mass is reduced compared to a surface mount machine, reducing the cost of the drive [12]. Thus, dual three-phase machine ensures a good compromise between additional complexity and potential benefits, making the integration with the conventional three-phase technology relatively simple [18]. Moreover, the adoption of a six-phase machine permits to reduce the phase current ratings, with significant benefits in terms of inverter and cooling system sizing.

The machine is designed for a maximum speed of 22.500 *rpm* and to sustain an overspeed of 27.000 *rpm* [10]. The performance of the motor, i.e. torque and power over the speed range, is shown in Figure 1.6 [10], while its specifications are listed in Table 2 [17]. They are derived from the end-user and driving requirements.

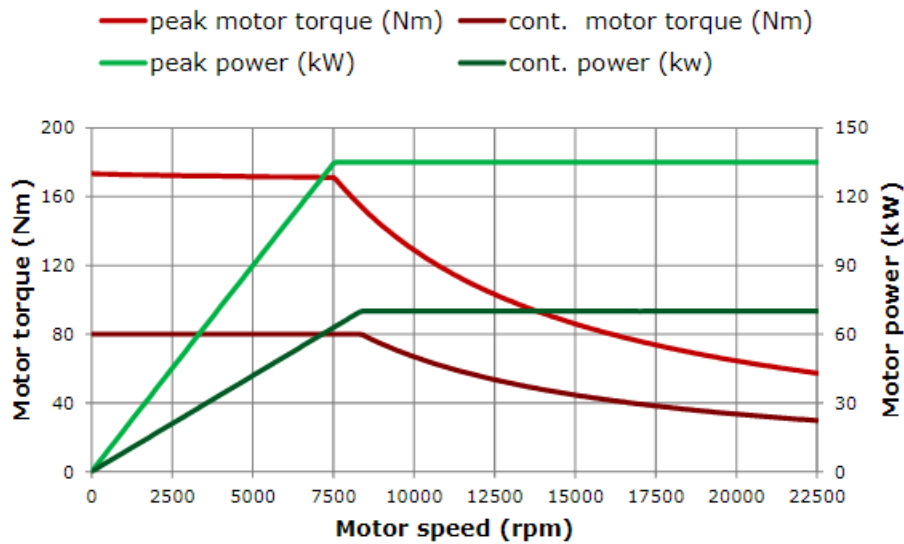


Figure 1.6: Motor performance specification (torque and power) for peak and continuous operation [10].

<i>SPECIFICATIONS MOTOR</i>	<i>VALUE</i>	<i>UNIT</i>
Motor topology	HSM (BPMSM)	
Phase number	6	
Winding technology	Formed litz wire (FLW)	
Max. operating motor speed	22.500	rpm
Peak torque	170	Nm
Peak power	135	kW
Continuous torque	80	Nm
Continuous shaft power	70	kW
Efficiency in nominal operation	> 96	%

Table 2: Topology, winding information and performance specifications of the e-motor.

1.1.1 IPMSM modeling

Regarding the spatial topology and number of phases, the FITGEN e-motor is a dual three-phase motor (Figure 1.7), to indicate that the machine has two sets of star-connected three-phase stator windings spatially shifted by 60 electrical degrees with isolated neutral points [18]. The first set phases are denoted with 1, 3, 5 and 2, 4, 6 for the second.

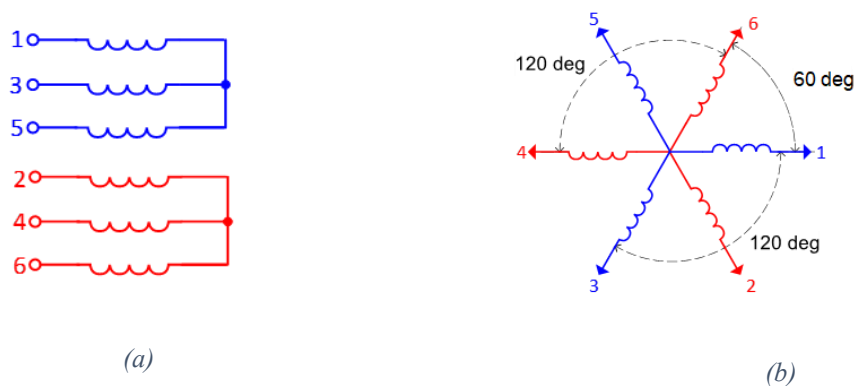


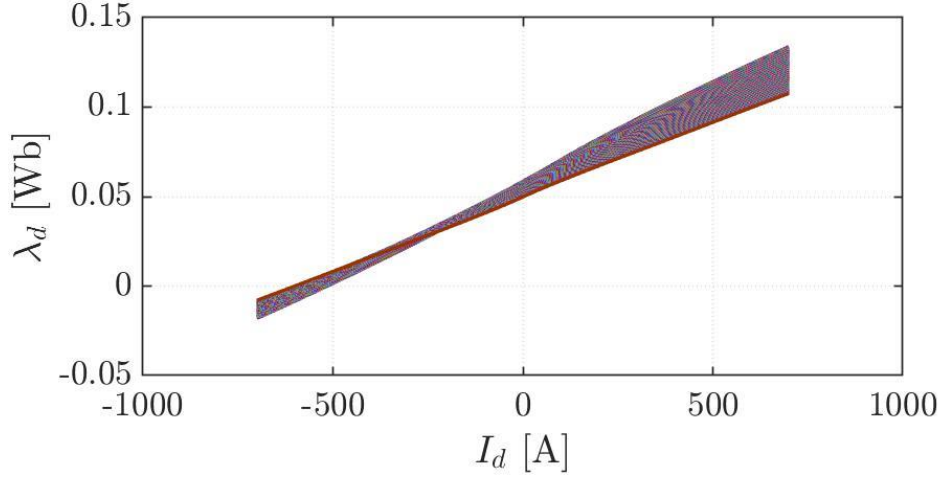
Figure 1.7: Inverter load (motor) comprising two independent three-phase systems (a), and electrical coordinate system (b) [19].

As specified more in detail in the following section, both winding sets are connected to a three-phase two level VSIs module. This solution is preferred over a six-phase inverter, that would require special vector control algorithms. The *DC*-link capacitors of the two inverter units are connected in cascaded configuration [20].

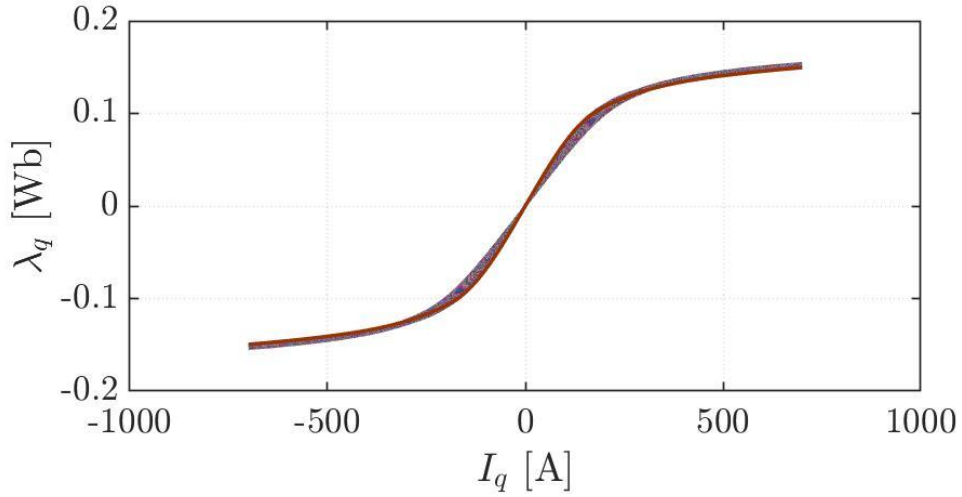
For a six-phase machine, the equation relating the phase voltages and currents is the following:

$$V = R_s I + \frac{dLI}{dt} + \frac{d\lambda_{PM}}{dt}, \quad (1)$$

where $V = [v_1, v_2, \dots, v_6]$ and $I = [i_1, i_2, \dots, i_6]$ are the phase voltage and current vectors, L is the 6x6 diagonal matrix representing the self and mutual inductance of the machine and the R_s is the stator resistance [19]. Taking into account the nature of the FITGEN machine, the effects of magnetic saturation and cross coupling in the machine's electrical behavior have an important impact and cannot be neglected. The inductance L not only varies according to the rotor electrical angle θ_e due to the variable magnetic reluctance of such rotor configuration, but also strongly depends on the stator current due to magnetic saturation. Moreover, also the per-phase magnetic flux linkage vector $\lambda_{PM} = [\lambda_{PM1}, \lambda_{PM2}, \dots, \lambda_{PM6}]$ generated by the permanent magnets varies with θ_e and the current [19]. In the FITGEN project, the *d*- and *q*-axis magnetic fluxes (Figure 1.18) and the inductances are obtained throughout simulations of a Finite Element Model (FEM) of the electric motor. The data are acquired by Brusa, which had the task of developing the electric motor in accordance with the transmission and inverter specifications. This approach allows to take into account the non-linear phenomena due to magnetic saturation.



(a)



(b)

Figure 1.8: BPMSM d and q fluxes according to FEM analysis. (a) Flux λ_d on varying the d -axis currents, (b) Flux λ_q on varying the q -axis current.

The electromagnetic torque generated by the motor is given by [19]:

$$T_{em} = \frac{1}{2} I^T \frac{dL}{d\theta_m} I + I^T \frac{d\lambda_{PM}}{d\theta_m} \quad (2)$$

where θ_m the mechanical angular position.

Both (1) and (2) give a sufficient mathematical representation of the electric machine. However, the model complexity and highly coupling issue, which influences the motor electromagnetic torque production, make it not appropriate for control system design. Therefore, to avoid drawbacks such as cross coupling effect and unbalanced sharing between the winding sets, for modeling and control dual three-phase PMSM, vector

transformations are applied. This approach allows to simplify the mathematical representation of the machine [20].

In particular, the machine model for salient pole dual three-phase PMSM is based on two transformation matrices, called T_1 and T_2 . The T_1 transformation (Figure 1.9(a)) is achieved by adapting the Clarke and Park transformations for a six-phase symmetric PMSM. This transformation decomposes the original phase-variable of the machine, i.e. current, voltages and fluxes, according to their harmonics components. In particular, neglecting the homopolar component, the T_1 matrix allows to decompose the system into two decoupled synchronous reference frames: the D_1-Q_1 plane (capital lettering is used to distinguish them from conventional three-phase d-q reference frames, i.e. rotor frames [18]), contains the fundamental components, while the 5th and 7th harmonics are mapped into the D_2-Q_2 reference frame (anyway, this condition holds only for a perfectly symmetrical case, since any imbalance between the winding sets causes the fundamental components and all the harmonics to appear in both reference frames [18]). The transformation matrix T_1 (3) consists of the stationary frame decoupling matrix and the rotation matrix and is given by [19]:

$$T_1 = \frac{1}{3} \begin{bmatrix} \cos\theta_r & \cos(\theta_r - \alpha) & \dots & \cos(\theta_r - 5\alpha) \\ -\sin\theta_r & -\sin(\theta_r - \alpha) & \dots & -\sin(\theta_r - 5\alpha) \\ \cos(5\theta_r) & \cos(5\theta_r - 2\alpha) & \dots & \cos(5\theta_r - 10\alpha) \\ -\sin(5\theta_r) & -\sin(5\theta_r - 2\alpha) & \dots & -\sin(5\theta_r - 10\alpha) \\ 1 & 0 & \dots & 0 \\ 0 & 1 & \dots & 1 \end{bmatrix} \quad (3)$$

Since zero sequence current components cannot flow, they can be neglected after the transformation. Using (3), the original phase-variable presentation of the machine is transformed into two decoupled two-axis synchronous reference frames. Thus, applying (3), for example, to the phase currents gives four independent current components (4) to be controlled in two different reference frames [18].

$$\begin{bmatrix} i_{D_1} \\ i_{Q_1} \\ i_{D_2} \\ i_{Q_2} \end{bmatrix} = T_1 [i_{a_1} \ i_{b_1} \ i_{c_1} \ i_{a_2} \ i_{b_2} \ i_{c_2}]^T \quad (4)$$

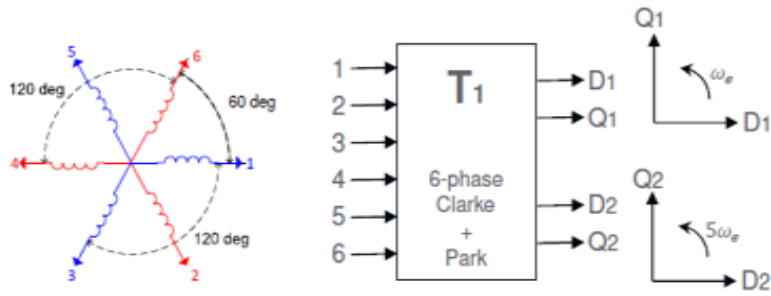
The T_2 transformation consists of applying the conventional magnitude invariant three-phase Clarke and Park transformations to each three-phase set. The application of such transformation projects the system into the d_1-q_1 and d_2-q_2 planes, each one related to

one of the three-phase winding sets. This transformation is illustrated in figure 1.9(b), and is given by [19]:

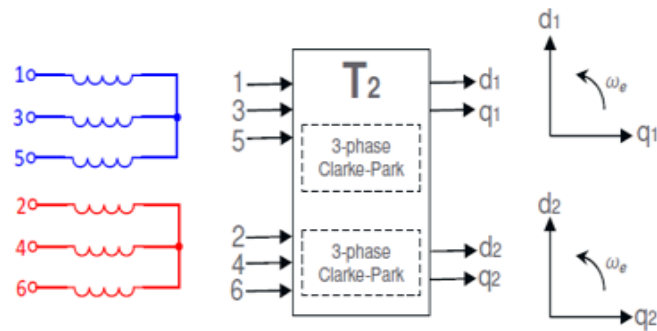
$$\begin{bmatrix} P_{3ph}(\theta_r) & \mathbf{0}_{3 \times 3} \\ \mathbf{0}_{3 \times 3} & P_{3ph}\left(\theta_r - \frac{\pi}{3}\right) \end{bmatrix}, \quad (5)$$

where $P_{3ph}(\theta_r)$ is the conventional three-phase Clarke-Park transformation.

The T_2 transformation ensures to control independently each three-phase current, but subject to cross-coupling effects, which make a good dynamic performance hard to achieve. Therefore, to avoid cross coupling problems and unbalanced current sharing between the winding sets, different reference frames are considered for model and control purposes: the first resembles the vector space decomposition (VSD) approach and the second one is a conventional d-q frame [18]. This approach ensures high-performance current control with the advantage of using the well-known and validate control techniques for the conventional three-phase PMSMs. Additionally, it allows ho handle and solve characteristic issues of dual three-phase machines, such as current harmonics and balanced current sharing.



(a)



(b)

Figure 1.9: Vector transformations used in the proposed controller: (a) Multiphase approach; (b) three-phase approach [19].

In particular, the $D - Q$ approach has the advantage of ensuring much simpler representation of the machine which can greatly benefit the control. Indeed, they are totally decoupled with respect to each other, which yield a very simple form for the machine equations [18]. Figure 1.10 clarifies the difference between $D - Q$ and $d - q$ reference frames.

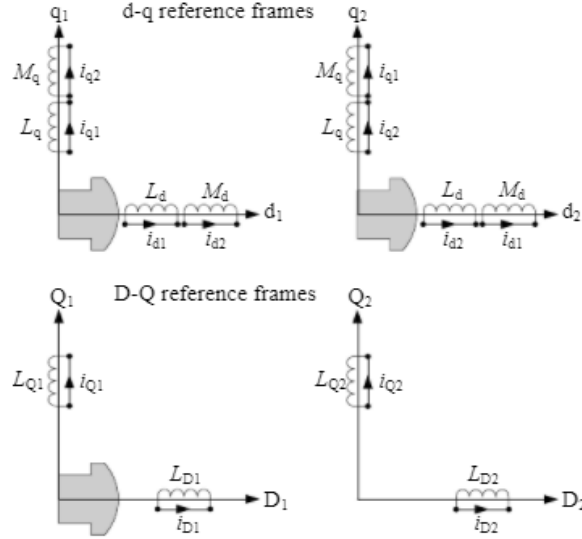


Figure 1.10: Conventional d - q reference frames (d_1 - q_1 for the first winding set and d_2 - q_2 for the second winding set) compared with the D - Q reference frames. Mutual inductance terms M_d and M_q describe the coupling between the frames in the d - q approach [18].

For current control, the most important equations of the machine are the stator voltage equations in both reference frames. By applying (3) to (1), the following vector model is given [19]:

$$\begin{cases} v_{D_1} = R_s i_{D_1} + L_{D_1} \frac{di_{D_1}}{dt} - \omega_e L_{Q_1} i_{Q_1} \\ v_{Q_1} = R_s i_{Q_1} + L_{Q_1} \frac{di_{Q_1}}{dt} + \omega_e (L_{D_1} i_{D_1} + \lambda_{PM1}) \end{cases} \quad (6)$$

$$\begin{cases} v_{D_2} = R_s i_{D_2} + L_{D_2} \frac{di_{D_2}}{dt} - 5\omega_e L_{Q_2} \\ v_{Q_2} = R_s i_{Q_2} + L_{Q_2} \frac{di_{Q_2}}{dt} + 5\omega_e (L_{D_2} i_{D_2} + \lambda_{PM5}) \end{cases} \quad (7)$$

where ω_e is the electrical angular speed of the rotor.

As can be noticed, in the vector model above both planes D_1 - Q_1 and D_2 - Q_2 are decoupled. The first set (6) is similar to the corresponding pair of stator voltage equations for a three-phase PMSM. The second set (7) differs from the first one only by the rotation at 5 times the angular speed. Thus, the used modeling approach offers simple dynamic equations for dual three-phase PMSM.

The last part to consider for machine modeling refers to the torque equation which can be straightforwardly obtained using a similar procedure as for conventional three-phase

machines. In particular, the electromagnetic torque T_{em} produced by dual three-phase PMSM can be computed as [19]:

$$T_{em} = 3p(\lambda_{PM}i_{Q_1} + (L_{D_1} - L_{Q_1})i_{D_1}i_{Q_1}) \quad (8)$$

where p is the number of pole pairs.

Similarly, by applying the T_2 transformation over (1) and (2), results in [19]:

$$\begin{cases} v_{d_1} = R_s i_{d_1} + L_d \frac{di_{d_1}}{dt} - \omega_e L_q i_{q_1} + M_d \frac{di_{d_2}}{dt} - \omega_e M_q i_{q_2} \\ v_{q_1} = R_s i_{q_1} + L_q \frac{di_{q_1}}{dt} - \omega_e L_d i_{d_1} + \omega_e \lambda_{PM} + M_q \frac{di_{q_2}}{dt} - \omega_e M_d i_{d_2} \end{cases} \quad (9)$$

$$\begin{cases} v_{d_2} = R_s i_{d_2} + L_d \frac{di_{d_2}}{dt} - \omega_e L_q i_{q_2} + M_d \frac{di_{d_1}}{dt} - \omega_e M_q i_{q_1} \\ v_{q_2} = R_s i_{q_2} + L_q \frac{di_{q_2}}{dt} - \omega_e L_d i_{d_2} + \omega_e \lambda_{PM} + M_q \frac{di_{q_1}}{dt} - \omega_e M_d i_{d_1} \end{cases} \quad (10)$$

$$\begin{aligned} T_{em} = \frac{3}{2} p [& \lambda_{PM}(i_{q_1} + i_{q_2}) + (L_d - L_q)(i_{d_1}i_{q_1} + i_{d_2}i_{q_2}) \\ & + (M_d - M_q)(i_{d_1}i_{q_2} + i_{d_2}i_{q_1})] \end{aligned} \quad (11)$$

It should be noted that the planes $d_1 - q_1$ and $d_2 - q_2$ for this model are coupled by the terms M_d and M_q . Therefore, the voltage, current and torque equations are more complex with respect to the three-phase motor ones. Moreover, both planes rotate at the same speed, but there is a $\frac{\pi}{3}$ -radians offset between them. Both planes can produce torque, as shown by (11) [19].

Lastly, the mechanical behavior of the machine must be modelled. To this purpose, the conventional rotating mass model has been used, where speed dynamics are given by:

$$T_e - T_l = J \frac{d\omega_m}{dt} + B\omega_m \quad (12)$$

where T_l is the load torque, J is the inertia moment of the rotating masses, and B is the viscous friction coefficient.

1.2 SiC inverter

The power rating of the inverter needs to meet the required level for the machine and driven load. However, the limitation on the power rating of semiconductor devices doesn't allow to increase the inverter ratings over a certain range. Thus, due to nonavailability of high-voltage and high-power switches, innovative techniques and new control strategies allowed to develop different viable multilevel converters. The whole idea is to use low- or medium-voltage devices where employing switches of reduced rating, obtaining converters that can process higher power at high voltage, making possible to use machine with more than three phases.

This is in line with the FITGEN aim in which the two three-phase sets of a dual three-phase PMSM are fed by two independent three-phase VSIs, whose DC -link capacitors are connected in cascaded configuration (Figure 1.11) [19].

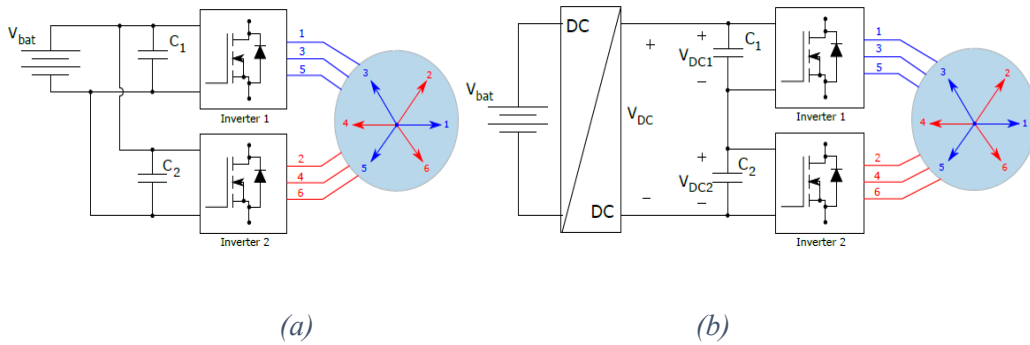


Figure 1.11: General diagram of the dual three-phase IPMSM drive architecture for a winding displacement of $2\alpha=\pi/3$: (a) conventional configuration, (b) cascaded DC -link capacitors with DC/DC converter [19].

In particular, an inverter topology consisting of two cascaded sub-inverters, denoted as inverter cells, is used for FITGEN. Each inverter cell is essentially a hard-switching, two-level, three-phase inverter (Figure 1.12), with a DC -link voltage of $400V$ and three-motor phase connections.

The concept of cascaded interconnecting two traditional three-phase VSCs to produce a multilevel converter has the advantage that each inverter cell has a blocking voltage of $V_{DC}/2$. This allows to use semiconductors with a blocking voltage of $650V$ while still maintaining the high total DC -link voltage in the $800V$ range required for fast DC -charging compatibility. The voltage across the two inverter-cell capacitances V_{DC1} and V_{DC2} needs to be balanced during active operation, by regulating the power circulating through each

three-phase set of the drive, guaranteeing an adequate motor torque regulation. Indeed, the best overall dual three-phase motor performance, i.e., good efficiency and torque quality, can be achieved when a balanced current sharing between the winding sets is ensured [20].

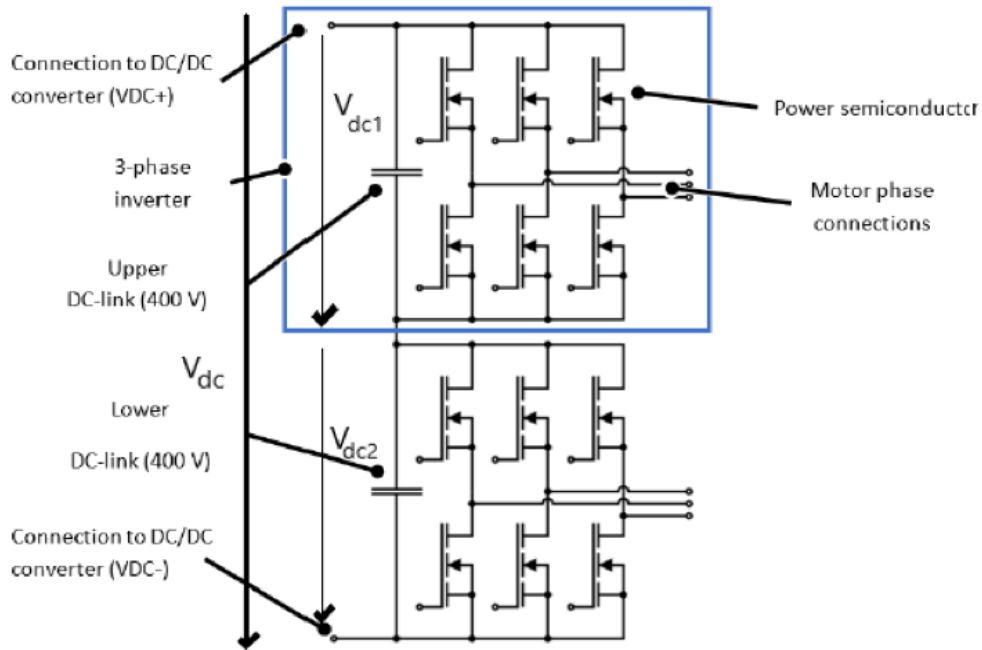


Figure 1.12: Cascaded topology of the inverter used in FITGEN showing the two inverter cells and the six-phase motor connections.

The six-phase inverter was custom designed with the aim of fulfilling various FITGEN requirements regarding performance, power density and efficiency and to be deeply integrated with the BPMSM. Indeed, the choice of wide band-gap SiC power MOSFETs is due to the greater power density and efficiency achievable with significant volume reduction compared to an IGBT inverter counterpart, representing the best choice for power conversion application [6]. Additionally, thanks to the higher switching frequency enabled by SiC components, the motor power losses should be reduced [14]. This allowed to achieve a highly compact drive, suitable to be mounted in A-segment EVs.

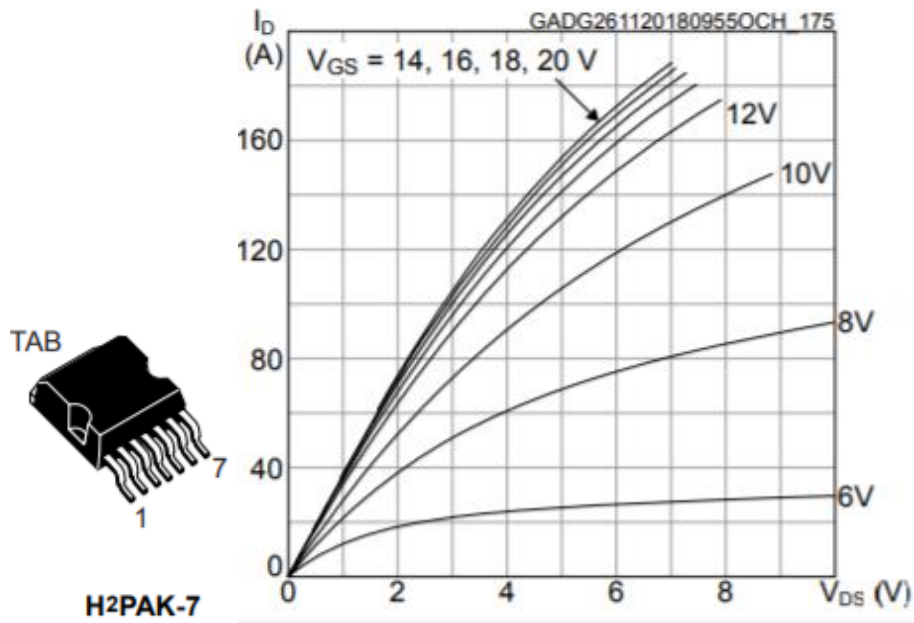


Figure 1.13: Adopted SiC power MOSFET and its rated conduction characteristic at 175° [15].

A selection of the most important target specifications of the FITGEN inverter is listed in Table 3 [17]. The DC-link voltage range is from 470 V to 840 V with a nominal DC-link voltage of 650 V.

SPECIFICATIONS INVERTER	VALUE	UNIT
Topology	Two levels, hard switching	
Phase number	6	
Semiconductor technology	SiC power MOSFET	
input voltage Range (DC-side)	470 – 840	V
Max. input current (DC-side)	200	A
Peak output current (RMS, per phase)	235	A
Continuous output current (RMS, per phase)	120	A
Efficiency in nominal operation	> 98	%

Table 3: Topology, semiconductor technology and target specifications of the inverter.

1.3 DC/DC converter

Based on the need of an embedded compatibility with *DC* fast charging stations and of maximum efficiency achievement, in many hybrids and full electric vehicle applications the question about the proper *DC*-link voltage level arises. To this purpose, the FITGEN project makes use of an efficient *DC/DC* conversion stage, which consists of a bidirectional non-isolated multilevel *DC/DC* converter, insert between the automotive battery and the six-phase inverter. The BRUSA commercial product BDC-546 is adopted (Figure 1.14), which is an automotive bidirectional boost converter, characterized by a rated efficiency of 98.9 %. It is functionally integrated into the FITGEN e-axle [6]. This means that the device is not changed but a control scheme is developed for the whole e-axle.



Figure 1.14: Picture of BDC-546 DC/DC converter [16].

The specifications of the *DC/DC* converter are listed in Table 4 [17].

<i>LV AND HV POWER SUPPLY</i>	<i>VALUE</i>	<i>UNIT</i>
Semiconductor technology	Si IGBT	
Battery input voltage range	50 – 600	V
Max. input current	400	A
HV output range	150 – 750	V
Peak output power	180	kW
Efficiency in nominal operation	98.9	%

Table 4: Input and output specifications of the *DC/DC* converter used for FITGEN.

During traction mode, the high voltage DC/DC converter steps-up the battery voltage (rated 400 V), creating a controlled DC -link with a maximum rating up to 750 V. Highly dynamic performance of the BPMSM at high speed are allowed, through a DC -link optimal control, which enables instantaneous optimization of the voltage level in traction. Indeed, the output voltage of the DC/DC , supplying the six-phase inverter, is online adapted depending on the motor operating conditions (speed and torque) to ensure control stability and contemporary minimizing the Joule losses [6]. The evaluation of such voltage adaptation strategy is the main focus of this thesis. A dedicated control strategy, which combine the inverter and DC/DC control, is covered in more detail in Chapter 2.

Moreover, with respect to fast DC -charging, the FITGEN architecture is made compatible with a wide range of high-power DC charging stations, adaptable with flexibility to chargers with nominal value up to 750 V DC .

1.4 Losses in the PE converters

As said, the core of the thesis is the evaluation and calibration of an optimized DC -link controller to minimize the power losses in both the traction inverter and the DC/DC converter. Therefore, a power losses estimation needs to be computed. The examined powertrain is supplied by a DC power source (battery) and converted via the DC/DC converter to a desired controlled DC -link voltage level. The electric machine is powered by a DC/AC inverter, which is fed by the DC -link voltage. The powertrain losses $P_{L,system}$ are corresponding to the individual component losses [23].

$$P_{L,system} = P_{L,DC/DC} + P_{L,DC/AC} + P_{L,EM} \quad (13)$$

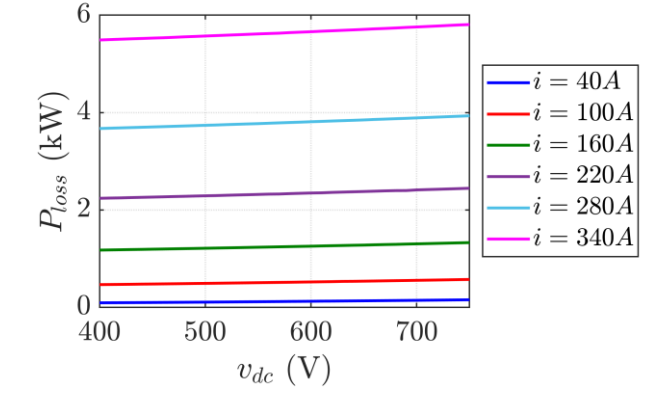
Although the motor control dynamic at high speed is significantly improved by the insertion between the battery and the traction inverter of the DC/DC converter, on the other hand, it necessarily introduces additional losses, affecting the EV efficiency. The system efficiency η is defined by the mechanical power P_{mech} of the electric machine and the DC power input to the DC/DC converter P_{batt} [23]:

$$\eta = \frac{P_{mech}}{P_{batt}} \quad (14)$$

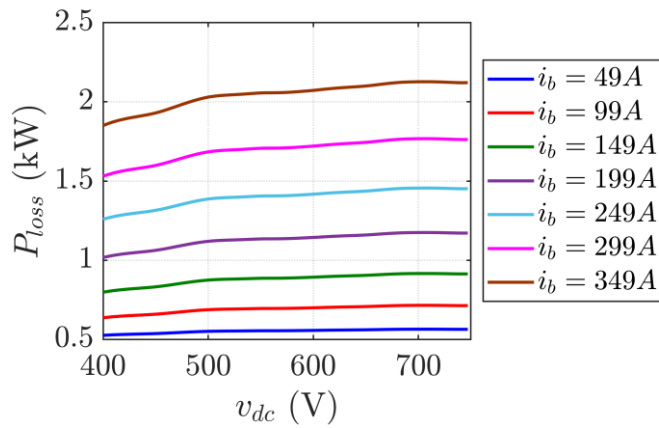
To increase the system efficiency, the component losses need to be reduced. Therefore, as a first step, it is important to define an accurate loss estimation model, based on the analysis

of the different losses at component level. The goal of the proposed variable DC-link voltage adaptation law is to reduce the loss in the *DC/DC* converter and in the six-phase inverter. Therefore, it requires evaluating the loss entity in the two converters when varying the *DC* link voltage v_{dc} in the full speed-torque range of the drive. The influence of the *DC*-link voltage on motor loss is considered negligible.

The losses at the *DC/DC* converter and at the *DC/AC* inverter can be diversified into two main components, i.e., the conduction losses and switching losses. The conduction losses are depending on the current and the temperature; the switching losses are related to the current and temperature as well, but also depend on the *DC*-link voltage v_{dc} and the switching frequency [23]. The key advantage is that the *DC*-link voltage can be set as a variable parameter in order to minimize the aggregate power loss (inverter + *DC/DC* converter) whatever the load power demand. Therefore, the resulting conversion efficiency will be maximized. Indeed, adjusting the *DC*-link voltage according to the load, e.g., reducing the v_{dc} at lower speed and torque motor operating points, can improve the overall efficiency [23]. The power loss characteristics of the both the traction inverter and the *DC/DC* converter on varying the *DC*-link for different phase current amplitude are reported in Figure 1.15 [9].



(a)



(b)

Figure 1.15: Power losses for different current levels: (a) in the 6-phase inverter, (b) in the DC/DC converter on varying the battery current, considering the rated battery voltage $v_b = 370V$.

It should be noted that for a given power of the motor, the losses in both converters increase with v_{dc} [9]. By boosting the DC-link voltage it is possible to reach a highly turning speed and to enlarge the range of the constant torque operation. In this way, the motor would enter in the flux weakening control region at a significantly larger speed. However, on the other hand, a lower DC-link voltage is beneficial in terms of lower converters' losses, since it reduces the switching losses on both the traction inverter and the DC/DC converter. In general, the conduction losses are instead weakly influenced by the v_{dc} in the case of the inverter and they increase, due to the higher current for a given output power, for the DC/DC converter. Overall, for the adopted DC/DC, the efficiency increases by reducing the DC-link voltage.

For the BDC546 converter, the efficiency and losses are obtained based on extended

datasheet given by BRUSA. The efficiency depends on the bus voltage v_{dc} and battery current i_{batt} . Therefore, the loss estimation must take into account also the battery SOC. However, it should be noted that some extrapolation of the data received from BRUSA was needed, so an approximation is introduced but it is acceptable for the study purposes. A more detailed analysis on the benefits of the adopted *DC*-link control strategy in terms of loss reductions will be discussed in chapter 3.

CHAPTER 2

2. Control strategy

In this chapter, a decoupled dual three-phase IPMSM control strategy in electric vehicle applications, under variable DC -link, is proposed. In general, control strategies can be highly influenced by the machine electrical parameters, leading to inaccurate regulation under electrical parameters deviations or, in more serious cases, instabilities. Additionally, the control of the machine can be lost if field weakening is not properly controlled and, as a consequence, uncontrolled regeneration is produced. Thus, during the whole propulsion system lifetime, advanced control techniques are needed to ensure electric vehicle drive controllability in the whole speed/torque operation range. In order to achieve these goals, a combination of a robust control strategy and a Look-up table/voltage constraint tracking, under both Maximum Torque per Ampere and Field Weakening operation, is proposed, improving the overall control algorithm accuracy under parameter deviations [21]. At first, the optimal motor operating point in the dq plane and the correspondent optimal v_{dc} are computed by using the FEM data of the machine, including MTPA tracking and FW operation, both under variable DC -link. Anyway, since these LUTs are computed based on the motor model, the calculated v_{dc}^* setpoint strongly depends on accurate knowledge of its parameters, so it is considered unreliable for practical implementation. Moreover, the proposed torque control strategy not only takes into account the cross-coupling effects of the machine but also incorporates input voltage balancing capabilities.

Additionally, an optimized DC -link controller is incorporated in the proposed design to increase the conversion efficiency by online regulating the DC -link voltage of the traction inverter, improving the overall motor control performance. The design procedure of the controller has been discussed below. The proposed DC -link adaptation technique is almost independent of the motor parameters and torque/speed control strategy; therefore, its usage is allowed in a wide number of applications. To prove it, the adopted DC/DC control was tested when combined with two different torque control techniques, namely Current Vector Control-Field Oriented Control ($CVC - FOC$) and Direct Flux Vector Control ($DFVC$). Moreover, each of them has been tested both in three-phase and six-phase configuration [9].

2.1 Motor control

To guarantee a successful control of the dual three-phase PMSM drive with such cascaded DC -link configuration, an active DC -link balancing strategy is required, to equally distribute the voltage at the output of the DC/DC converter. Therefore, the adopted controller aims to independently regulate the power consumed (or delivered in case of regenerative braking) by each three-phase set. In this way, if the desired value ($V_{DC}/2$) is not perfectly tracked by one of the input voltages of the inverter cells, the control will react correcting the deviation, by increasing or decreasing the power consumed by the respective three-phase set. Moreover, to achieve a good dynamic performance, the coupling effects between the three-phase sets need to be also considered [19].

To this purpose, instead of implementing an independent torque control loop for each three-phase set, which is treated as an independent machine, a *multiphase torque control* strategy is considered. The benefit regards the application of the *double three-phase torque control*, consisting in the implementation of the well-known and validated control techniques for three-phase machine for independently control each three-phase set. This approach allows to handle the DC voltage balancing need, while avoiding the drawback of not addressing the coupling between sets [19]. Indeed, the problem of unbalanced current sharing requires the machine to be controlled in two separate reference frames simultaneously. In this way the machine can be seen as two separate three-phase systems with independent current controls [20].

Figure 2.1 [19] shows the related block diagram of the proposed controller, in the case of Current Vector Control-Field Oriented Control approach. However, as has already mentioned, to confirm the independence of the variable DC -link strategy from the motor control also the Direct Flux Vector Control is tested. Both the torque motor control strategies are covered in the later sections of chapter 2.

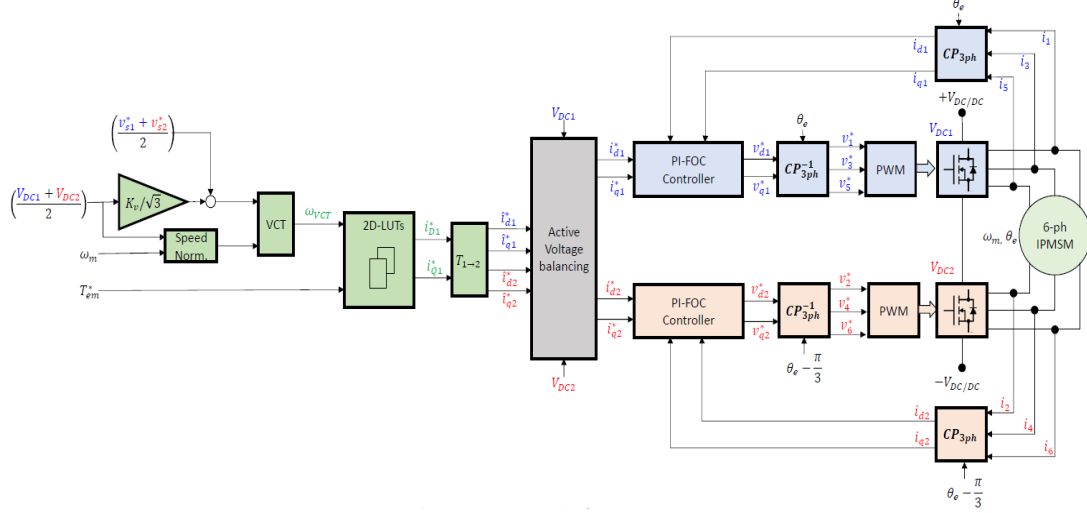


Figure 2. 1: Block diagram of the multiphase torque control approach.

The torque control block scheme consists of majorly three parts. The first stage is responsible of the optimal current set-points generation, based on the required torque and the actual operating point, i.e., motor currents, stator voltage and speed. The second one implements the active voltage balancing operation. Lastly, the third stage includes the synchronous current regulation loops [19]. To successfully control the dual three-phase machine in the whole speed/torque operating range, optimal current set-points are computed using the FEM data of the machine with a relatively low computational burden, and stored into LUTs. In the case of *multiphase torque control* approach the current generation is done in the $D - Q$ frames. The dimensions required for reference current vectors i_D^* and i_Q^* generation in an LUT-based approach depends on the specific application. In general, for automotive IPMSMs, since the optimal current set-points are dependent on the reference torque, the DC -link voltage and the mechanical speed, tridimensional 3D-LUTs are needed [19]. Instead, the rotor temperature is not considered in industrial applications as its precise estimation is more complex and generally the deviations produced by temperature effects can be considered acceptable, so no compensation action is need to perform. Thus, the LUTs dimension can be reduced to only two inputs, i.e., the torque reference, which is mandatory, and the mechanical speed, which must also be considered in systems where FW operation is required. Moreover, the DC -link voltage feedback is also needed in systems where V_{DC} can vary, as is the case of a battery powered EVs [21]. However, it is possible to eliminate this magnitude from the LUT by using the speed normalization (ω_{norm}) concept, where the mechanical speed ω_m and the DC -link voltage V_{dc} are correlated as follow [21]:

$$\omega_{norm} = \frac{1}{\mu} |\omega_m| = \frac{V_{DC}^{norm}}{V_{DC}} |\omega_m|, \quad (15)$$

where V_{DC}^{norm} is the normalized voltage for which the current set point LUTs have been computed.

However, although LUT-based approach is commonly preferred thanks to its simplicity and low computational cost, it has the limit of tuning the control algorithm for a specific set of electrical machine parameters. This means that under parameter deviations, it may eventually loss control due to an incorrect regulation of FW operation, i.e., exceeding the stator voltage limitation and leading to an uncontrolled energy regeneration [21]. Indeed, the drawbacks of this approach can be summarized as follow [22]:

- Depending on their size and number of dimensions, LUTs can require a relatively high amount of memory;
- The torque control may be affected by irregularities due to machine electric parameters variations which may be caused by manufacturing tolerances, machine ageing or temperature changes. This leads to possible instabilities in the Field Weakening (FW) region.

For that reason, to take into account the machine parameter variations issues, it is of interest to include an online field weakening control loop, i.e. a Voltage Constraint Tracking (*VCT*) feedback is used. Figure 2.2 shows its structure, where the average of the reference stator voltages (v_{s1}^* , v_{s2}^*) and *DC*-link input voltages (V_{DC1} , V_{DC2}) are considered to feed the VCT loop [19].

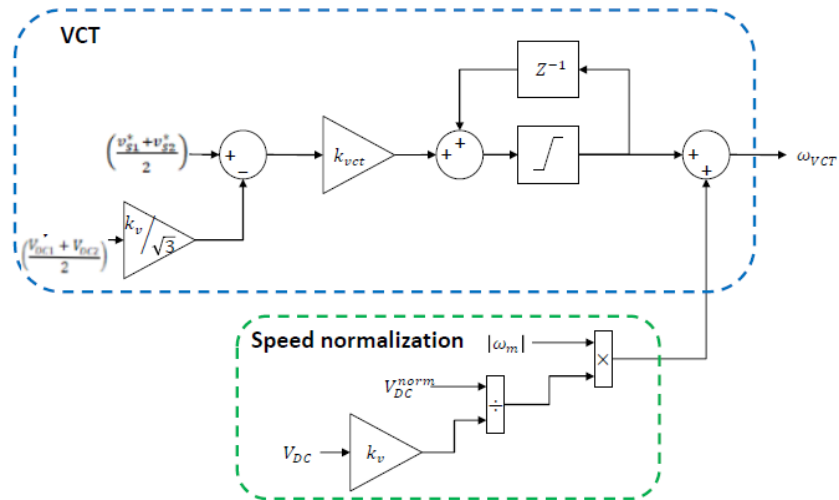


Figure 2. 2: Block diagram of the VCT feedback loop [19].

The VCT regulator aims to keep the stator voltage vector under the maximum voltage constraints in the FW and MTPV regions, by varying the mechanical speed fed to the 2D-LUTs, based on the error produced between the current control reference stator voltages average and the voltage limit [22].

The main advantage of the proposed method is that it only modifies the theoretically or experimentally predefined optimum set points when it is required, maintaining the LUT values when deviations are sufficiently small to allow machine controllability [22]. Moreover, this strategy does not require to know any machine parameters since only the two constants k_v and k_{vct} need to be defined. In particular, the first one is selected from $0.8 < k_v < 1$ to maintain the stator voltage under the voltage limit margin, while $k_{vct} > 0$ is tuned to correctly adjust the VCT regulator dynamics. Then, the modified speed (ω_{VCT}) and torque setpoint (T_{em}^*) are the inputs to the 2D-LUTs, resulting from the optimization of the current references for the different motor operating regions. In particular, the optimum currents LUTs are evaluated from phases flux data computed from the IPMSM FEM model. As the currents $i_{D1} - i_{Q1}$ are the responsible for producing torque, only two LUTs are required. Once the optimal set-points $i_{D1}^* - i_{Q1}^*$ are calculated, they are transformed into the $d_1 - q_1$ and $d_2 - q_2$ planes [19]. This is done thanks to the transformation $T_{1 \rightarrow 2}$ [19]:

$$\begin{bmatrix} d_1 \\ q_1 \\ h_1 \\ d_2 \\ q_2 \\ h_2 \end{bmatrix} = \begin{bmatrix} 1 & \cos(6\theta_r) & -\sin(4\theta_r) & 0 & 0 \\ 0 & -\sin(6\theta_r) & \cos(4\theta_r) & 0 & 0 \\ 0 & 0 & 0 & 1 & 0 \\ 1 & -\cos(6\theta_r) & \sin(6\theta_r) & 0 & 0 \\ 0 & \sin(6\theta_r) & \cos(6\theta_r) & 0 & 0 \\ 0 & 0 & 0 & 0 & 1 \end{bmatrix} \begin{bmatrix} D_1 \\ Q_1 \\ H_1 \\ D_2 \\ Q_2 \\ H_2 \end{bmatrix} \quad (16)$$

Then, the resulting current references are modified to ensure the DC-link voltage balancing, based on the error between the measured DC-link voltage of each cell and the desired reference ($V_{DC}/2$). For simplicity, it has been chosen to modify only the current set-points i_{q1}^* and i_{q2}^* , even if it causes a small deviation from the MTPA locus in the torque region. Indeed, the discrepancy is lower than 5% and is considered acceptable. Figure 2.3 [19] shows the block diagram of the proposed algorithm.

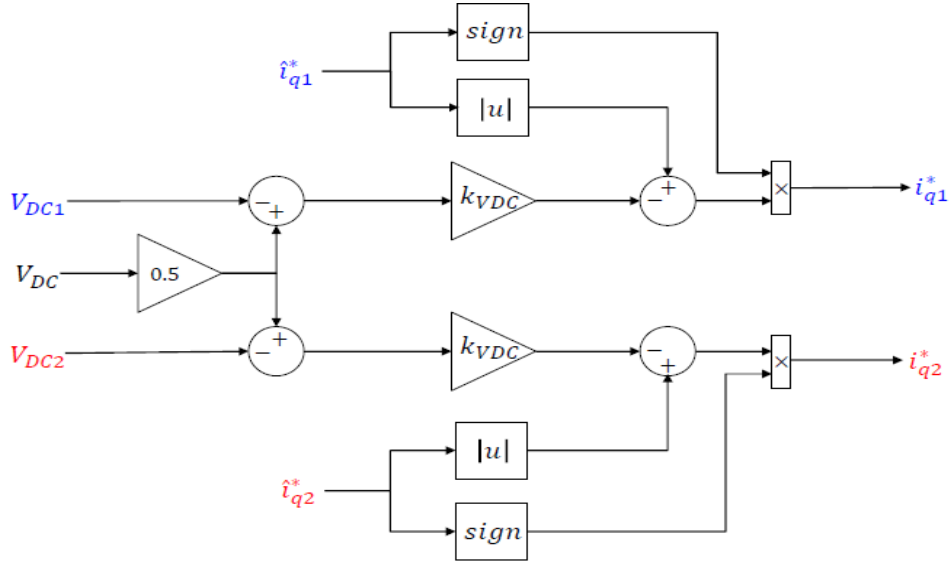


Figure 2. 3: Block diagram of the proposed active voltage balancing algorithm.

The last stage of the double three-phase torque controller features two conventional current control loops, one for each three-phase set, which include the Proportional-Integral controllers (PI), decoupling feed-forward terms and anti-windup schemes. Then, the voltage references are transformed from dq components to the respective three-phase values. Finally, PWM blocks synthesize the firing pulses for each inverter cell [19].

2.1.1 IPMSM torque control regions under variable DC-link

Due to inverter current rating and the available DC-link voltage, an IPMSM drive exhibits speed and torque constraints. These limitations can be expressed in terms of current and voltage as follows:

$$i_d^2 + i_q^2 \leq I_{max}^2, \quad (17)$$

$$v_d^2 + v_q^2 \leq \frac{V_{DC}^2}{3} \quad (18)$$

In order to satisfy both the limits given by the inverter and the thermal machine requirements, the relation (17) must hold, where I_{max} is the maximum output current of the inverter. That is, the current must be kept inside the limit circle shown in Figure 2.4. It should be noted that the current limit curve (17) is equivalent to a circumference of radius I_{max} in the stator currents dq plane [22]. Once the limit is reached the current vector has to be reduced along path D for increasing speeds and decreasing battery voltages [24]. Moreover, in order to avoid the system to reach voltage overshoot, the motor voltage should be also restricted within a certain range (18). That is, the IPMSM can be operated

under constant torque as long as the required voltage does not exceed the maximum output voltage of the inverter which supplies the machine. The maximum inverter output is determined by the DC -link voltage, V_{DC} , and the type of PWM-modulation. The fully usage of the DC -link voltage is guaranteed by the modulation with zero sequence injection [24]. Thus, in a two-level three-phase Voltage Source Inverter (VSI) fed machine, the maximum achievable phase voltage for the linear modulation region (when PWM with third harmonic is adopted) is [22]:

$$V_{max} = \frac{V_{DC}}{\sqrt{3}} \quad (19)$$

It should be also noticed that, due to the different d - and q - inductances of IPMSM, the voltage constraint forms an ellipse instead of a circle, whose radius decreases when the motor speed increases (Figure 2.5(a)) [22]. Thus, the critical conditions of (17) and (18) are given by a “current limiting” circle and a “voltage limiting” ellipse as shown in the following Figure [24].

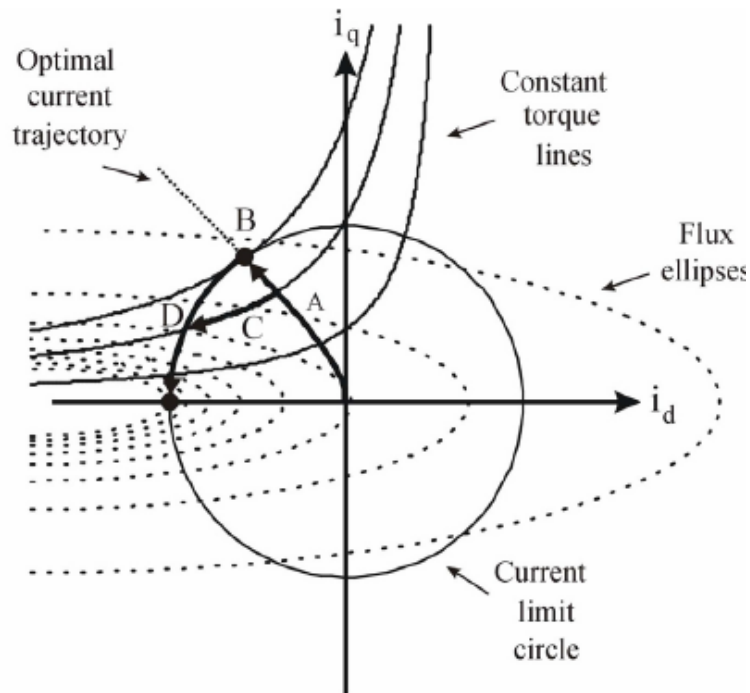


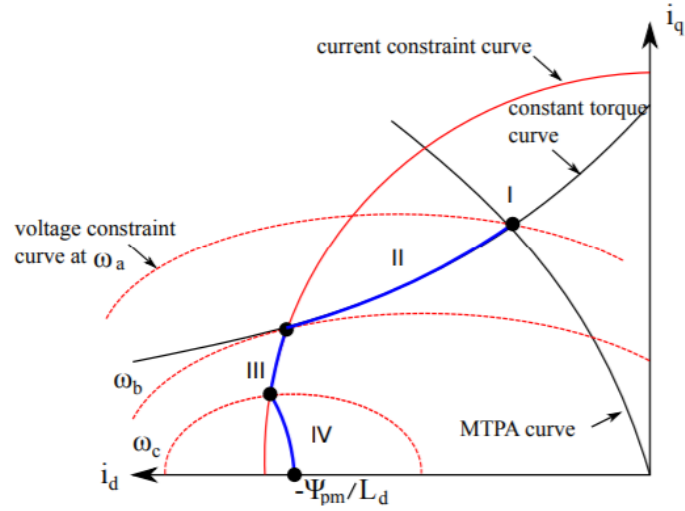
Figure 2. 4: Current circle diagram [24].

If field weakening operation is not used, the consequence of achieving the voltage limit is that the torque will fall to zero. In more serious cases, might be happen that the current controller becomes unstable. To prevent this allowing the drive to work for a wider speed range, field weakening must be used. Hence, it is necessary to limit the required stator voltage to the maximum output voltage of the converter. Field weakening with constant

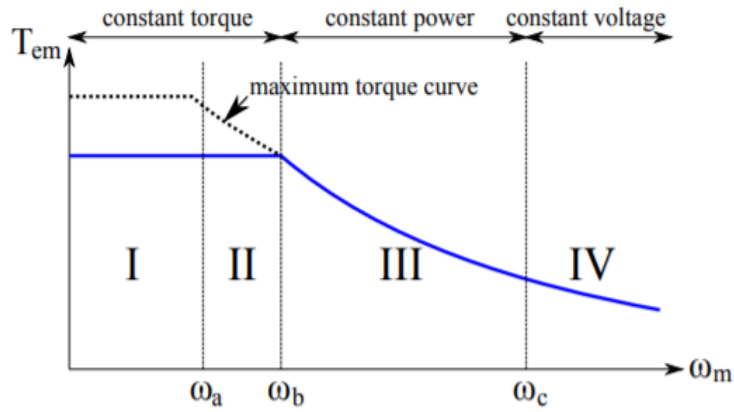
torque can be obtained by forcing the d -axis current away from the optimal current trajectory along path C in Figure 2.4. The d -axis current can be seen as a demagnetizing current opposing the flux from the permanent magnets keeping the voltage within the limit. The current in the field weakening region is not optimal, i.e. maximizes the torque-per-current ratio, but the machine can be operated with constant torque in a wider speed range [24].

According to these constraints and considering an arbitrary torque inferior to the maximum one, four optimum operation regions can be distinguished (Figure 2.5(a) and 2.5(b)) [22]:

- I. **Maximum Torque Per Ampere (MTPA) region.** The MTPA curve, existing in the stator current dq reference frame, ensures a maximum torque per applied current modulus (Figure 2.5(b), region I). Minimum ohmic losses (predominant at low speeds) are obtained if this curve is tracked.
- II. **Field weakening region without torque reduction.** The i_d current should be reduced to extend the speed operation region of an IPMSM. In a given region, this is achieved without losing torque capability, as i_q^* can be recomputed to keep the torque to the reference value (figure 2.5(b), region II). This region can be extended until the speed ω_b is reached (figure 2.5(a)), where the speed and current limit curves intersect with each other.
- III. **Field weakening region with torque reduction.** When current constraint circle is reached, the torque capability is reduced in FW operation (Figure 2.5(b), region III). In this region, the maximum torque can be achieved by positioning the current set point vector in the intersection between the voltage and current constraint curves.
- IV. **Deep field weakening region.** In this operation region, also known as Maximum Torque Per Voltage (MTPV) region, the torque production capability is maximized for a constant stator voltage value (Figure 2.5(b), operation region IV). The MTPV region only exists for a given IPMSM if $\frac{\psi_{pm}}{L_d} \leq I_{max}$ condition is fulfilled, and can be mathematically determined. Moreover, in this region the magnetic losses (predominant at high speeds) are minimized.



(a) Optimal trajectory of the stator currents in the dq plane taking into account the current and voltage constraints.



(b) Optimal trajectory of maximum torque regions for an arbitrary torque $T_{em} < T_{em}^{max}$: MTPA (I), field weakening (II), field weakening with torque reduction (III) and MTPV (IV).

Figure 2. 5: IPMSM optimal control trajectories and regions [22].

As a final remark, to keep the Joule losses at minimum, both the proposed motor control strategies, CVC-FOC and DFVC, act by forcing the operating point to lay on the MTPA locus below the base speed ω_b , while field weakening is needed at higher speed. Moreover, the high capability of moving to and from flux weakening conditions is a key requirement of the motor control strategy for operating successfully under variable DC -link. It should be noted that ω_b increases with the applied V_{dc} . When DC -link voltage increases, ω_{norm}

becomes lower than the real speed ω_m . This is equivalent to a displacement of the speed vs torque curve towards the right side (Figure 2.6), expanding the voltage limit. Conversely, the opposite occurs when the DC -link voltage is reduced [22]. Therefore, by adapting the V_{dc} , through the variable DC -link control, and so ω_b , the motor Joule losses are decreased, permitting to operate on the MTPA.

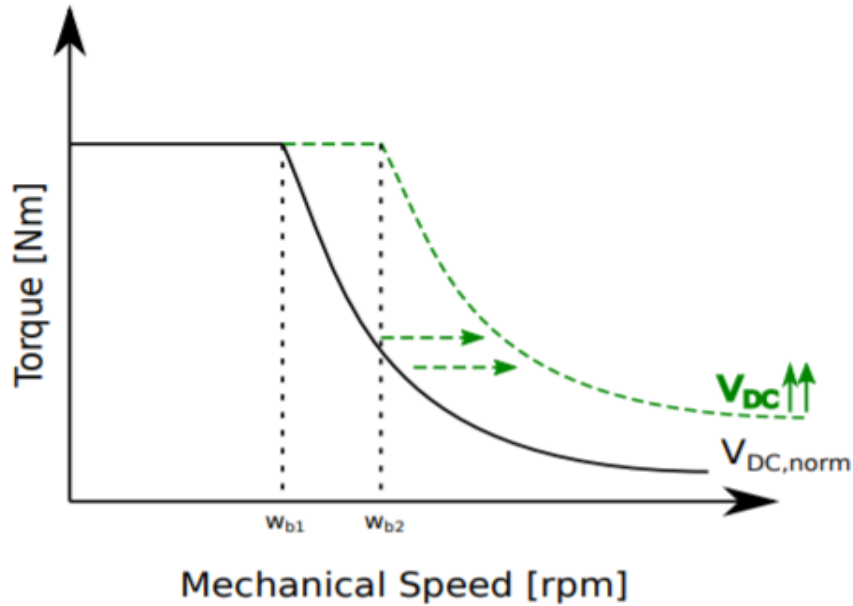


Figure 2. 6: Torque and speed curve in DC -link voltage variation [22].

Hence, as has already said, the normalized speed can be computed in case of variable DC -link voltage operation conditions and used as an input for a 2D LUT. The consequent benefit is that the amount of memory resources required to implement the algorithm in a microprocessor is highly reduced [22]. An algorithm is used to derive look-up tables for the current references, whose dimension can be reduced to two if, as has been mentioned before, the normalization speed is added to the control software. Depending on the torque reference, instantaneous vehicle speed and battery voltage, the aim is to produce current references for the current controller. The current references are defined to obtain an optimal current set point, so that the torque-per-current ratio is maximized, under the restriction of keeping the stator voltage and current limited [22]. Based on the measurements of the motor acquired by BRUSA, the algorithm scans all combinations of torque reference values, spanning from 0 to T_{max} , and mechanical speed values, spanning from ω_{min} to ω_{max} . Current combinations are chosen along the current limit circle and within the flux ellipses (path D in Figure 2.4) and stored in look-up tables, for both the direct and the quadrature current reference.

2.1.2 CVC- Field Oriented Control (FOC)

The most common control strategy in multiphase drives is the well-known *CVC*-Field Oriented Control method. Among the other features, it allows to achieve the desired torque-speed characteristics with good motor dynamic performance, by implementing mathematical transformation to decouple the PM motor torque generation and the magnetization flux components of stator current [26]. Figure 2.7 [9] depicts the adopted control strategy for a three-phase machine (it can be extended to the six-phase case with specific algorithms):

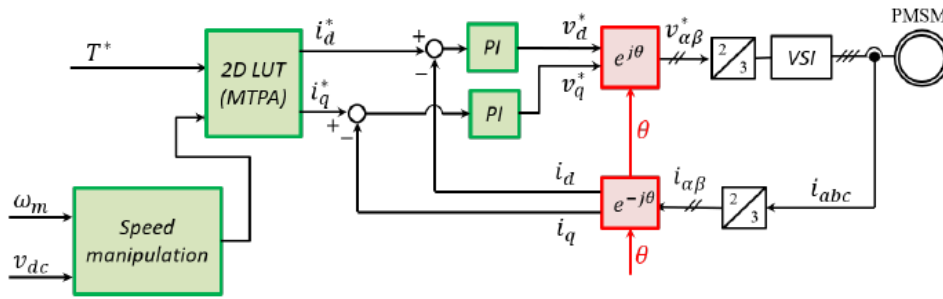


Figure 2. 7: Tested CVC-FOC.

The proportional integral (PI)- based FOC must be complemented with an optimal set-point current generation algorithm, required to control an e-drive system through the maximum efficiency points, including FW operation when needed. Hence, based on the precomputed LUT, the torque reference T^* can be translated into an optimal current vector i_{dq}^* , so that it lays on the MTPA locus at medium and low speed and moving to field weakening when the voltage reaches the maximum reference value [9]. As has been already mentioned, the determination of the reference current vector is based on the reference T^* , set by the user, the measured speed n and the measured v_{dc} , thus requiring Look-up Tables in three dimensions. However, in this implementation, to consider the v_{dc} variability, the complexity of the LUTs is reduced to two dimensions based on T^* and a manipulation of the measured speed, permitting a reliable torque control in flux weakening even under relevant *DC*-link variations.

By using current regulator, required current for a commanded speed can be regulated for the PMSM drive. Here the actual three-phase stator currents taken from the three-phase inverter is transformed into the $\alpha\beta$ components by the Clarke transformation module first and then into the dq ones by Park transformation. These two components thanks to the feedback current control approach are compared with their respective reference current.

The corresponding current error fed the two proportional–integral (PI) regulators, which is a suitable solution in EV for controlling the direct axis (d - axis) and quadrature axis (q - axis) current to obtain the desired reference torque. Hence, the control output, computed by PI controllers, is influenced by the controller error and is tuning by two main controlling parameters, i.e., K_p (proportional gain) and K_I (integral gain), for both the q - axis and d - axis current regulator. The values of both the scalar gains for current controller are given by the following equation.

$$K_p = L \cdot 2\pi f_{ci} \left(\frac{V}{A} \right), \quad (20)$$

$$K_I = K_p \cdot \frac{R}{L} \left(\frac{V}{As} \right), \quad (21)$$

where f_{ci} is the crossover frequency set at about 1/10 of the sampling frequency. The two tuning parameters K_p and K_I for q - axis current regulator are set to 1.13 and 213.18 respectively. Similarly, for d - axis current regulator the tuning scalar gains K_p and K_I are set to 0.18 and 35.53 respectively. The outputs of the PI regulators, i.e., v_q^* and v_d^* , are applied to the inverse Park transformation, obtaining the corresponding components in the $\alpha\beta$ stationary orthogonal reference frame. The stator voltage vector $v_{\alpha\beta}^*$ is the signals that drive the inverter. Then the inverter will supply the three-phase PMSM motor by the required current to achieve the command torque with command speed.

2.1.3 Direct Flux Vector Control (DFVC)

The second tested control technique implemented is the *DFVC*, where the two controlled variables are the flux linkage amplitude λ and quadrature current components i_{qs} , both closed loop imposed by dedicated PI controllers operating in stator flux coordinates (d_s, q_s), where the subscript “s” will refer to the stator flux reference frame [9]. In this case the regulation of the torque is made by means of one current component, responsible also of ensuring the inverter current limit satisfaction, as for current vector control. This control strategy has been applied for its inherent ability ease of flux weakening. Indeed, the motor voltage is easily controlled during FW operations with no need of current tables or flux references, but by upper saturating the reference flux amplitude depending on the motor speed and *DC*-link voltage. The *DFVC* allows also easy adaptation to a variable *DC*-link with no firmware modification [25].

Figure 2.8 [9] shows the block scheme of the direct-flux field-oriented control developed for a three-phase motor drive (it can also be extended to the six-phase case with dedicated algorithms).

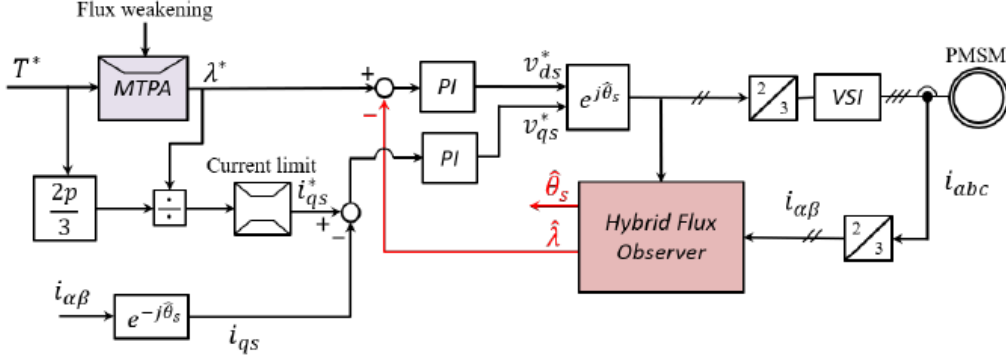


Figure 2. 8: Tested DFVC.

Starting from the reference torque, the flux amplitude set point are determined according to the MTPA lookup table, as said. The quadrature current reference i_{qs}^* is then calculated based on the torque and flux set points. The maximum current and maximum voltage limits are handled through a saturation block limiting the current and flux references. A closed-loop Hybrid Flux Observer (HFO) is also implemented for the flux linkage amplitude estimation, based on the current model and the integration of the back-electromotive force. The direction of the observed flux vector in stator coordinates $\widehat{\lambda}_{\alpha\beta}$ defines the d_s axis, shifted by the angle θ_s respect to the α direction. As usual, the q_s axis is 90° ahead of the d_s direction [9].

The vector control block scheme of Figure 2.8 contains also two proportional–integral regulators for the closed-loop control of the two selected variables. The flux amplitude λ regulation is actuated by the direct voltage component v_{ds} , from the q_s -axis. In particular, the closed-loop bandwidth is directly imposed by the proportional gain of the PI flux controller with no influence of magnetic saturation. The reference flux amplitude λ^* is instead set based on MTPA locus, as said, and flux weakening is implemented by directly limiting λ^* based on the measured speed and DC -link voltage [9]:

$$\lambda_{max} = \frac{\frac{v_{dc}}{\sqrt{3}} - R_s i_{qs} \cdot \text{sign}(\omega)}{|\omega|} \quad (22)$$

The torque can be regulated by controlling the q_s current component at a given flux via the quadrature voltage component v_{qs} . The bandwidth of the q_s -axis current loop is imposed by the proportional gain of the PI current controller and the inductance L_q .

The maximum current and maximum voltage limitations are handled by considering two saturation blocks ensuring to keep the i_{qs} and λ references under the required constraints. In particular, as can be seen, another DFVC advantage refers to the possibility of directly limiting the maximum motor current through the control of the quadrature current reference [25].

2.2 Variable DC-link Control Strategy

The developed *DC/DC* control algorithm aims to minimize the v_{dc} without affecting the motor control performance, i.e., ensuring efficient operation of the traction drive even under variable *DC-link* voltage, including MTPA and field weakening (FW) range and without limiting the torque control bandwidth. Simultaneously, the upper and lower voltage constraints of the *DC/DC* converter must be respected. In particular, the output v_{dc} on the motor side must be at least 10% higher than the input voltage v_b (battery side). Depending on the battery State of Charge (SOC), v_b is bounded between 320 V and 420 V, so the lower limit of v_{dc} is between 352 V and 462 V. A lower limit of 400 V was imposed in the simulation tests for simplicity.

$$v_{dc} \geq 1.1 \cdot v_b \quad (23)$$

The upper limit of the saturation block is fixed by the maximum operating v_{dc} achievable by the *DC/DC* converter without derating, i.e., 750 V.

$$v_{dc} < 750 \quad (24)$$

At first, the *DC/DC* control was developed for the equivalent three-phase motor drive and then extended to the dual-three phase case, without affecting its high performance. Whatever the adopted algorithm, the output of the torque motor control is the reference voltage vector in stationary reference frame $v_{\alpha\beta}^*$, which is then translated to the reference phase voltages v_{abc}^* . The $v_{\alpha\beta}^*$ vector is used as input of the variable *DC-link* control block and used to define the reference voltage command v_{dc}^* . For standard three-phase PWM or

Space Vector modulation techniques, the maximum allowed amplitude of the voltage vector (peak of phase voltage) is given by [9]:

$$|v_{\alpha\beta}^*|_{max} = \frac{v_{dc}}{\sqrt{3}} \quad (25)$$

Therefore, based on the $v_{\alpha\beta}^*$ computed by the motor control algorithm, the minimum required DC -link voltage is:

$$v_{dc} \geq \sqrt{3} \cdot \sqrt{(v_{\alpha}^*)^2 + (v_{\beta}^*)^2} \quad (26)$$

The two control strategies, namely “**Control type 1**” and “**Control type 2**”, proposed for automatically adapting the DC -link voltage during operation, without relying on motor data, are described in the following sections. Among the two controls, the first one has a simpler implementation and calibration (only two parameters need to be tuned), but requires a tradeoff between motor control dynamic and power loss minimization at medium speed. Similar dynamic performance but a further optimization of the DC -link voltage control is instead ensured by the Control type 2, at the cost of a more complicated calibration procedure. It should be noted that the proposed DC/DC control strategies can be used whatever the adopted torque control strategy and can be implemented independently by DC/DC converter structure, which can be integrated with the inverter or not [9].

2.2.1 DC/DC Control type 1

The block scheme of the variable DC -link control of *type 1* for a generic three-phase drive is depicted in Figure 2.9 [9].

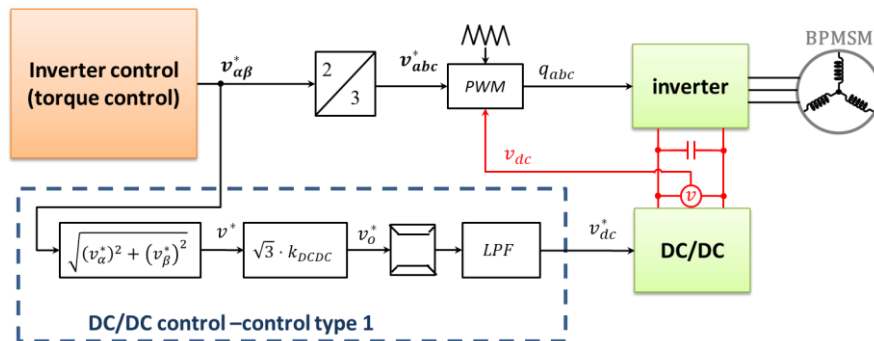


Figure 2. 9: Block scheme of the DC/DC control – type 1.

It should be noted that the determination of the v_{dc}^* command vector is based on the reference voltage vector in stationary reference frame $v_{\alpha\beta}^*$, which is the motor torque control output. In particular, the amplitude of the $v_{\alpha\beta}^*$ vector is required for computing the v_o^* voltage signal, which is given by [9]:

$$v_o^* = \sqrt{3} |v_{\alpha\beta}^*| \cdot k_{DCDC}, \quad (27)$$

where at steady state, $k_{DCDC} > 1$ is the margin between the actual v_{dc} and its minimum value permitting to the inverter to synthesize the reference $v_{\alpha\beta}^*$ voltage vector. Indeed, the v_{dc} must be sufficiently larger than the theoretical minimum value indicated by (26). The numerical value of the k_{DCDC} factor depends typically on the motor control dynamic which is intended to achieve by considering a certain safety margin with respect to the inverter phase voltage. In this way, at a steady state, even during flux weakening operation, the motor control does not exploit the full DC -link voltage. As an example, by setting the scalar gain $k_{DCDC} = 1.1$, the 10% voltage margin are guaranteed. The effect of the k_{DCDC} on the power losses in the traction inverter and in the DC/DC converter is also taken into account for the calibration purpose.

Then, v_o^* signal needs to be saturated between the minimum and maximum voltage (defined by the DC/DC operating limits), and filtered by a Low-Pass Filter (LPF), obtaining the v_{dc}^* reference voltage command. Finally, as has already said, the v_{dc}^* is communicated from the MicroAutoBox, containing the DC/DC control algorithm, to the VCU and then from the VCU to the DC/DC converter. This causes a significant delay of ≈ 25 ms between the generation of the v_{dc}^* command and its execution. Another source of delay to be considered is due to the finite bandwidth of the DC/DC converter voltage loop, presenting a step response settling time of 3 ms. Lastly, it should be noted that the main parameters of the DC/DC control type 1 that need to be tuned are limited to the scalar gain k_{DCDC} and the cut-off frequency of the LPF, proving the simplicity of the implementation of proposed variable DC -link control [9].

2.2.2 DC/DC Control type 2

The block diagram of the DC/DC control *type 2* for a generic three-phase machine is reported in Figure 2.10 [9].

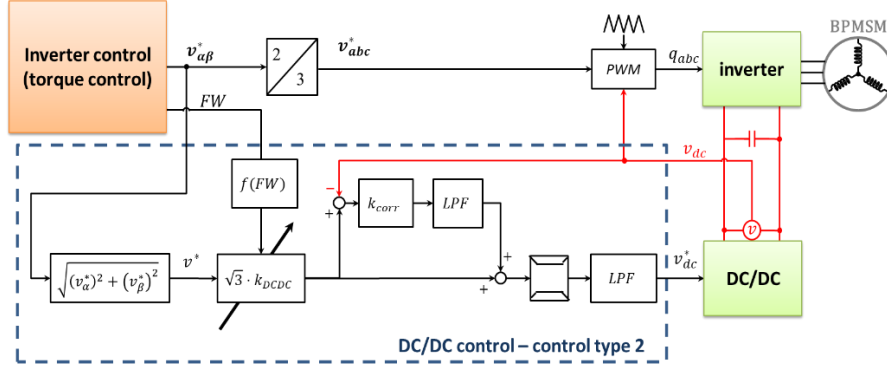


Figure 2. 10: Block scheme of the DC/DC control – type 2.

As can be noticed, the *DC/DC* control type 2 is derived from type 1 with two additional features. The first refers to a variable scalar gain k_{DCDC} . Based on the $f(FW)$ function, the k_{DCDC} value is online adapted depending on the actual operating region of the motor. Specifically, the FW is set to 0 if the torque control is working on the MTPA locus, whereas it a flag of $FW=1$ is imposed in case of field weakening speed range. The second improvement consist of a feed-forward term added based on the measured v_{dc} feedback. In particular, it is obtained from the error between v_{dc} and the reference v_{dc}^* . Then, the difference between the v_o^* signal and the measured v_{dc} is multiplied by the scalar gain k_{corr} and added to v_o^* . As has already seen for the *DC/DC* control type 1, the final stage of the controller includes a saturation block, based on the *DC/DC* converter operating limits, and a Low-Pass Filter (LPF). Hence, the obtained reference v_{dc}^* is given by [9]:

$$v_{dc}^* = LPF(v_o^* + k_{corr}(v_o^* - v_{dc})) \quad (28)$$

Finally, the v_{dc}^* command voltage is communicated to the *DC/DC* converter and executed, as said, with a significant delay, which must be considered at calibration stage. Moreover, such type of controller allows to improve the *DC/DC* control dynamic during transient, i.e., when $v_{dc} \neq v_{dc}^*$, without significantly affecting the steady state performance [9].

2.2.3 DC/DC Control for 6-phase Drive

The variable *DC*-link control can be extended to the six-phase case with dedicated and more complex algorithms, which do not significantly interfere with its dynamic performance. Specifically, the input voltage vector $v_{\alpha\beta}^*$ to the *DC*-link control block is, in this case, the aggregate of the reference voltages of the two three-phase sets $v_{\alpha\beta,1}^*$ and $v_{\alpha\beta,2}^*$. The combination law relating the two voltage vectors depends on the type of

connection between the two three-phase inverter units. In the case of cascade connection, the input to DC/DC controller is the total DC -link reference voltage vector, given by [9]:

$$|v_{\alpha\beta}^*| = |v_{\alpha\beta,1}^*| + |v_{\alpha\beta,2}^*| \quad (29)$$

As has already said, it is necessary for the torque control to include an accurate voltage balancing algorithm, allowing a reduced voltage discrepancy between the two three-phase inverters, by equally split the DC -link voltage. The control block scheme is reported in Figure 2.11 [9].

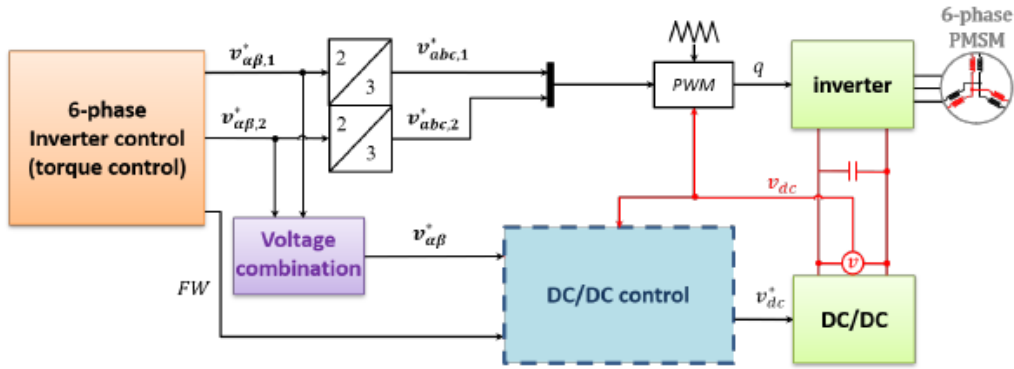


Figure 2. 11: Block scheme of the proposed DC -link control strategy extended to a 6-phase drive.

Overall, depending on the different topology of multiphase converters, a proper combination law of the reference voltage vectors can be easily determined, demonstrating the proposed DC/DC control strategy to be suitable for a wide range of applications. It is important to remark that the control calibration, bandwidth and performance are not modified respect to the three-phase case [9].

2.2.4 Control calibration

This section focuses on the optimal calibration roles of the proposed DC -link adaptation strategy, valid both for the three-phase and for the six-phase cases. The calibration procedure focuses on a tradeoff between a fast motor control dynamic with reliable safety margin and power loss minimization. The DC/DC control type 1 requires tuning two parameters: the scalar gain k_{DCDC} and the cut-off frequency of the LPF, demonstrating the simplicity in the implementation of this adaptive DC -link control. The calibration of the gain k_{DCDC} focuses on a good control performance achievement at steady state with an optimal voltage utilization on one hand, and a conversion efficiency improvement on the other. The higher the gain adopted, the larger safety margin is imposed, permitting to

maintain stable torque control under faster motor acceleration, but also the less are the benefits in terms of power losses at medium speed. Indeed, as said, the switching losses depend on the DC -link voltage; thus, with a larger v_{dc} the aggregate losses (traction invert + DC/DC converter) are not minimized. The second parameter requiring calibration is the LPF cut-off frequency, to avoid unstable or underdamped response but it limits the DC/DC control dynamic. Indeed, such filter is also related to the bandwidth of the DC/DC control, i.e. high bandwidth of the DC/DC control is obtained with a light LPF. This allows energy saving maximization by correctly imposing the minimum required v_{dc} . However, the feasible DC -link control bandwidth is limited by the communication delay and the internal DC/DC voltage bandwidth delay, as has been already mentioned, and by the possible interaction with the motor control. Indeed, a fast DC/DC control dynamic might interfere with the motor control algorithm and inverter modulation. For this reason, to ensure a reliable system, the LPF calibration should be optimized by keeping the cut-off frequency sufficiently slower than the torque control bandwidth. It could be suitable set the LPF frequency at 30 Hz, to be compliant with a wide range of motor torque control strategies. However, assuming a sufficient robustness of the torque motor control under fast DC -link variations, a higher control bandwidth can be also acceptable, at the cost of possible oscillations in the DC -link voltage response [9]. The DC/DC control type 2 also requires calibrating the LPF frequency and the k_{DCDC} value. However, in this case, the k_{DCDC} is split in two gains k_{DCDC}^{min} and k_{DCDC}^{max} . Specifically, the safety margin is set to a minimum value $k_{DCDC} = k_{DCDC}^{min}$ when the drive is operating on the MTPA, and linearly increased up to the maximum value $k_{DCDC} = k_{DCDC}^{max}$ under flux weakening operation. In this implementation, the minimum gain value k_{DCDC}^{min} is set to 1.1, whereas $k_{DCDC}^{max} = 1.2$. This approach allows to overcome the inherent limit of the control type 1, i.e., the tradeoff between good motor dynamic performance under sharp speed transient and minimum system power losses. Another parameter the control type 2 requires to be tuned is the scalar gain k_{corr} . With a proper calibration of k_{corr} , the v_{dc} feedback allows achieving high dynamic control performance even under a lower k_{DCDC} value. This permits to improve the system efficiency in the medium speed range [9].

CHAPTER 3

3. Simulation results

Simulation results for investigating the performance of the BPMSM drive under variable *DC*-link voltage for different operating conditions, such as variable load operation and/or sudden change of speed are discussed in chapter 3. The simulations are carried out in Matlab-Simulink environment, according to the motor, *SiC* inverter and *DC/DC* converter requirements given in chapter 1. The *DC*-link control was tested when combined with two motor control strategies, namely *CVC – FOC* and *DFVC*. For each case, the *DC/DC* control was tested for the equivalent three-phase motor drive first, considering the two three-phase sets of the reference machine connected in parallel. Then, the *DC/DC* control has been extended to the six-phase case. Moreover, the results shown in the current chapter are referred to the proposed control strategy when conventional LUT-based approach is used for current set point determination. As has already seen, the optimal current set point LUTs have been precalculated using the FEM data of the machine, to achieve good torque and FW control performance in the whole operating range.

3.1 Simulink models

The results come from tests validated in Matlab-Simulink environment, by using accurate modeling of the electrical machine and power electronic converters. The model of the electric drive has been simulated including the cross-coupling and magnetic saturation effects of the dual three-phase machine. Moreover, as has been mentioned in the dedicated chapter, since the *DC/DC* converter adopted for FITGEN is a commercial BRUSA product, and it is not possible to have complete access to it, a black box is used in Simulink environment to model it. A white noise with $\pm 5 V$ amplitude is also added to the output of the *DC/DC* converter to model the aggregate switching ripple of the two converters (*DC/DC* and inverter), which leads to ripple on the *DC*-link voltage. The Simulink model of the *DC/DC* converter is shown in Figure 3.1, where the input is the reference *DC*-link voltage command v_{dc}^* and the output the obtained v_{dc} . Moreover, the input voltage varies from 320 to 420 *V*, depending on the battery SOC, and 750 *V*. However, an equivalent three-phase motor is considered, which is supplied by half of the *DC*-link. Therefore, the default maximum and minimum v_{dc} are set at 200 *V* and 375 *V* respectively.

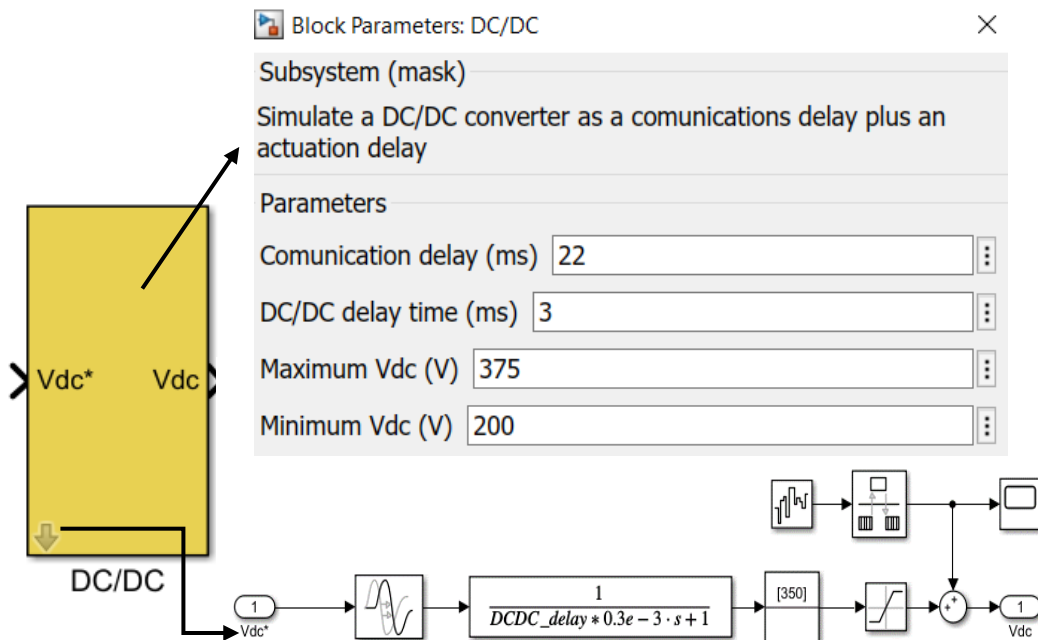


Figure 3. 1: Model of the DC/DC converter: mask, parameters and subsystem.

As can be noticed, pre-defined default values can be set from the block mask:

- **Communication delay (ms):** it simulates the delay for communicating the reference voltage command v_{dc}^* to the *DC/DC* control unit. It is estimated to be approximately $22ms$ of delay as a default value ($10ms$ from the inverter control unit to the VCU, $10ms$ from the VCU to the *DC/DC* control unit and other few ms for computation inside the VCU);
- **DC/DC delay time (ms):** actuation delay of the *DC/DC*. According to the BDC546 datasheet, the default value imposed is $3ms$, which is the response time to a step input;
- **Maximum v_{dc} (V):** maximum v_{dc} which allowed by the *DC/DC*;
- **Minimum v_{dc} (V):** minimum v_{dc} which can be obtained from the *DC/DC*.

The *DC/DC* control is implemented in the *DC/DC* control block, which is a triggered subsystem. Figure 3.2 shows the model of the *DC/DC* control in the Simulink environment.

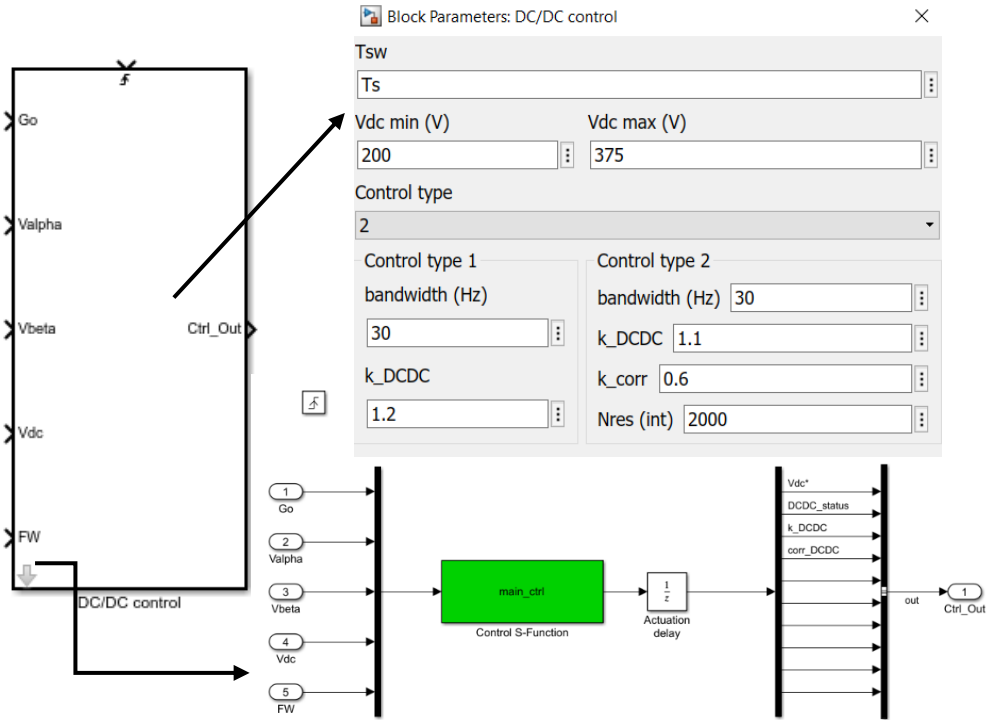


Figure 3. 2: Model of the DC/DC control: mask, parameters and subsystem.

It should be noticed that every control parameter can be set from the block mask, with predefined default values. There are two new parameters in the block mask with respect to the previous case:

- **T_{sw}** : interrupt service routine period, normally equal to the switching period;
- **Control type**: to select the control type 1 or 2. Depending on the type chosen, the parameters required for the calibration of the *DC*-link control algorithm are listed at the bottom of the block mask and need to be define.

3.2 DC-link control for a 3-phase Drive

This section details the calibration roles of the proposed *DC*-link adaptation strategy, valid for both the three-phase and the six-phase cases. In particular, the results of the *DC*-link control for a three-phase motor drive were reported first, and then the control has been extended to the six-phase case. The simulations are run under different load and speed conditions.

3.2.1 DC/DC control type 1

The first simulated working cycle is depicted in Figure 3.3, where the motor is controlled in DFVC under three-phase configuration. The test was performed with an LPF cut-off frequency of 30 Hz and a scalar gain $k_{DCDC} = 1.15$. The upper subplot depicts the torque required by the motor (the black line represents the reference torque command) and speed transient, whereas the flux and current amplitude and the maximum flux λ_{max} (black line), are shown in the middle subplot. The third one depicts the DC-link voltage command imposed by the DC/DC controller and the minimum DC-link voltage required to synthesize the reference $v_{\alpha\beta}^*$ (input voltage vector $v_{\alpha\beta}^*$ amplitude multiplied by $\sqrt{3}$).

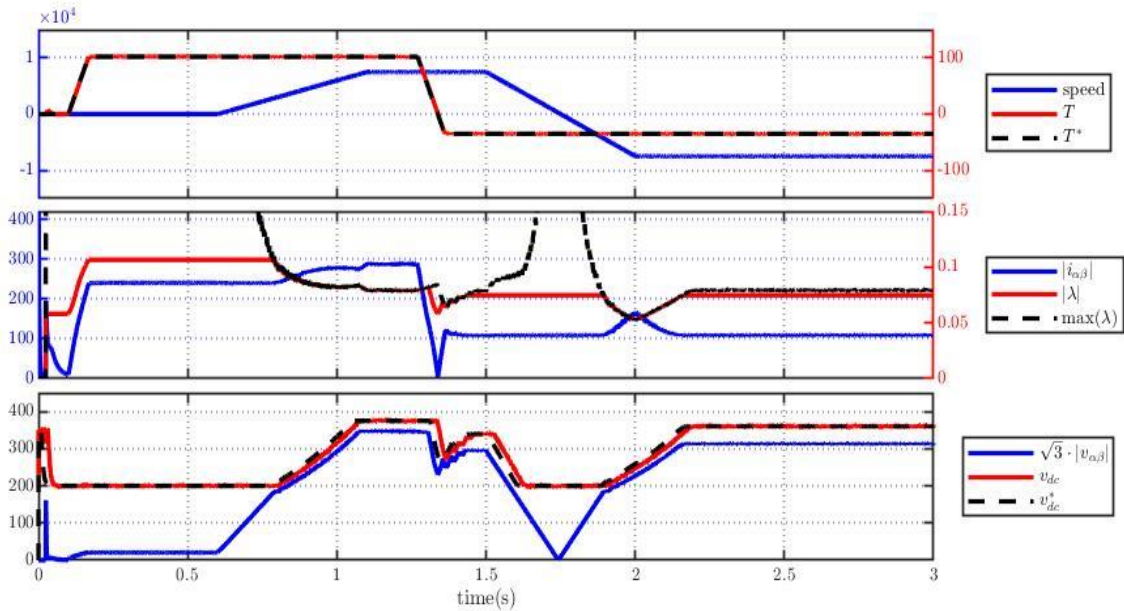


Figure 3. 3: Simulation of the DC/DC control- light flux weakening cycle. Calibration: $k_{DCDC} = 1.15$; LPF cut-off frequency = 30 Hz.

It should be also noted the measured DC-link voltage v_{dc} (red line) follows the reference signal v_{dc}^* (black line) with a remarkable delay since it is required a certain time to communicate and execute the DC-link voltage command.

As can be noticed in Figure 3.3 the three-phase drive presents three regions of steady state operation. At standstill, i.e. at zero torque and speed, and for $t < 0.6$ s, i.e. when a 100 Nm torque step is imposed at zero speed, the minimum DC-link voltage is sufficient for controlling the machine along the MTPA locus, therefore the command v_{dc}^* imposed by the DC/DC control is keeping at its minimum value (200 V). it should be also highlighted that DFVC operates on the MTPA when the reference flux is below the flux limit, whereas

it imposes field weakening when $\lambda = \lambda_{max}$ [9]. At medium speed, for $0.6 \text{ s} < t < 1.2 \text{ s}$, the minimum v_{dc} is not enough to keep the machine operating on the MTPA region, thus, the motor control would tend to weaken the flux. To avoid this, the *DC/DC* control reacts by gradually increasing the *DC*-link voltage. In this way it is possible to maintain the motor working point on the MTPA, delaying the FW operation. At $t \geq 1.2 \text{ s}$, i.e. for a speed of 5600 rpm (50 Km/h) up to 7500 rpm (68 Km/h), the v_{dc}^* is saturated to its maximum allowed value (375 V). Since no further increase of the *DC*-link voltage is possible, the torque control gradually weakens the flux as the MTPA locus cannot be tracked anymore. This results in a lower flux amplitude and higher current for the same torque, producing higher Joule loss. At $t = 1.5 \text{ s}$, a sharp speed reversal is applied, moving back to the MTPA locus. At this point, the *DC/DC* control tends to decrease the v_{dc}^* , minimizing the losses in the converters. For negative speed values, the control reacts similarly.

Figure 3.4 depicts another example of simulation results for the three-phase configuration drive, controlled with DFVC, but under a deep flux weakening operating cycle. The test was performed with the same LPF calibration as Figure 3.3, i.e. a cut-off frequency of 30 Hz , but with a scalar gain of 1.2. The simulation starts at zero torque and speed. Then a torque step of 35 Nm is demanded by the motor control whereas a sharp acceleration to the maximum operating speed (22 krpm) is imposed. Despite the high speed the torque transiently goes to zero before becoming negative. The speed is reversed at more or less 1.8 s , and then increased in negative direction. It should be noticed that the higher speed imposed a deeper flux weakening correspond to. Moreover, the same considerations of the previous operating cycle are still valid, i.e. the v_{dc} is correctly imposed by the *DC* controller, demonstrating that it is not limiting the motor control performance either under deep FW operation. In particular, the *DC*-link is keeping close to its minimum limit for lower speed values, thus reducing the required voltage, and is increased when the speed increases in negative direction. In turn, the motor control is stable even under severe transients and FW conditions.

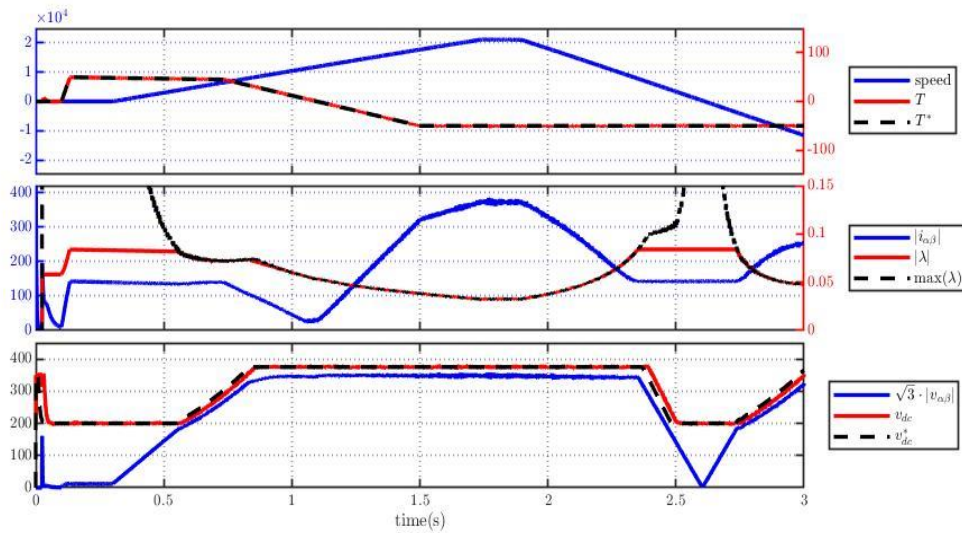
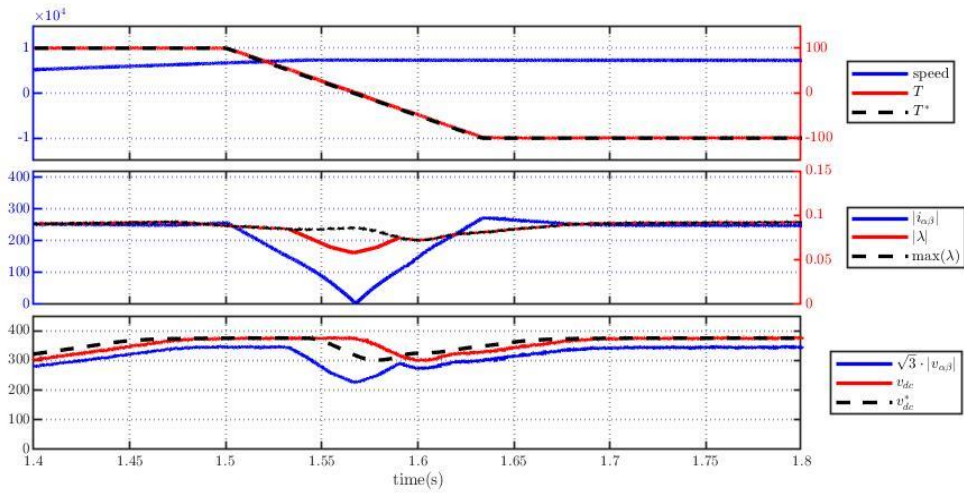
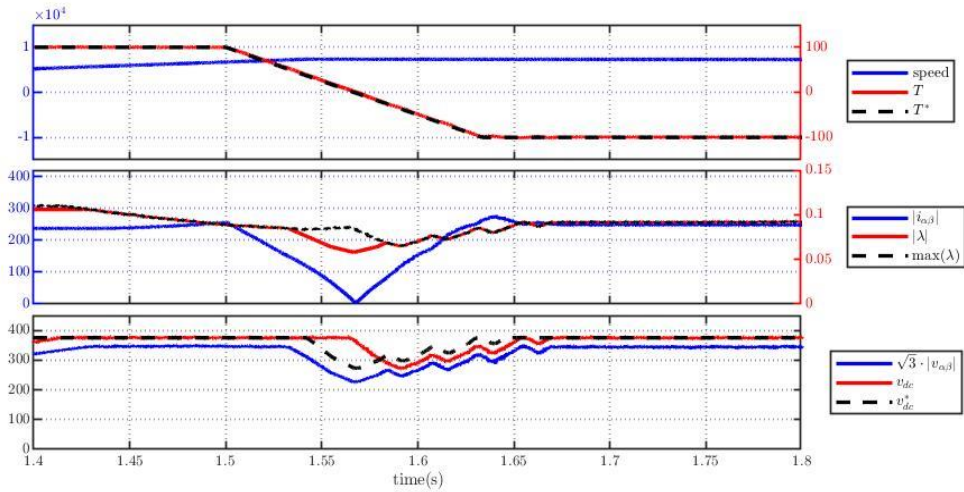


Figure 3. 4: Simulation of the DC/DC control- deep flux weakening cycle. Calibration: $k_{DCDC}=1.2$, LPF cut-off frequency =30 Hz.

The effect of LPF calibration is depicted in Figure 3.5, where the motor is still controlled in DFVC in three-phase configuration. Both cases report a sharp torque reversal from 100 Nm to -100 Nm under an increasing medium speed. The Figure 3.5(a) shows the response for a LPF cut-off frequency of 10 Hz while for the test reported in Figure 3.5(b) the filter was set at 200 Hz.



(a)



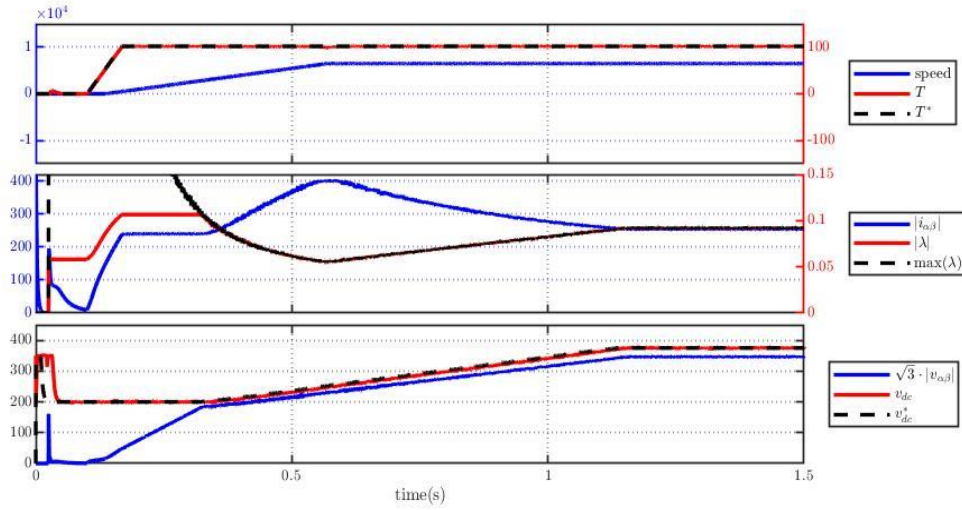
(b)

Figure 3. 5: Simulation of the DC/DC control –Response to torque reversal at 7500 rpm for $k_{DCDC} = 1.1$ and LPF cut-off frequency of a) 10 Hz, b) 200 Hz.

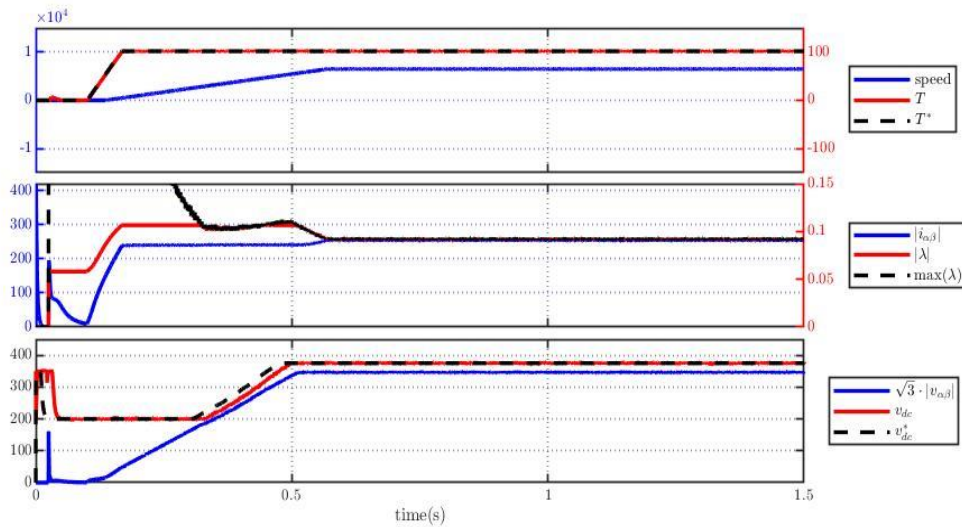
As has already been mentioned, the filter is necessary for defining the bandwidth of the DC/DC control and avoiding instability or under-damped response at medium speed. With respect to the first test, in the second one a significant the DC-link voltage ripple under a sharp torque variation can be noticed, but it does not interfere with the motor control algorithm. In particular, the torque control accuracy is ensured by the DFCV inherent capability of following the torque set-point, but it may be critical in other types of control, such as CVC [9].

The effect of the k_{DCDC} calibration on the control performance during transient is shown instead in Figure 3.6, where two simulations under the same load cycle but with different

gain values, are depicted. In particular, the tests were run under a sharp torque ramp to 100 Nm and fast acceleration, with the same LPF calibration, i.e. a cut-off frequency of 50 Hz, and a scalar gain $k_{DCDC} = 1.1$ and $k_{DCDC} = 1.2$ respectively.



(a)



(b)

Figure 3. 6: Simulation of the DC/DC control –Response to a sharp torque ramp and fast acceleration. Calibration: LPF cut-off frequency of 50 Hz and scalar gain a) $k_{DCDC} = 1.1$
b) $k_{DCDC} = 1.2$.

It should be noticed from Figure 3.6(a) that a lower scalar gain k_{DCDC} requires higher current overshoot during transient (400 A), since the variable DC-link control is too slow

in increasing v_{dc} . Thus, under these conditions, unavoidably deeper field weakening on the motor is necessary, leading to higher current amplitude. In this case, the DC/DC control takes almost 1.2 s to get the DC -link voltage close to the maximum. Conversely, if $k_{DCDC} = 1.2$ is set (Figure 3.6(b)), stable torque control under faster acceleration is ensured. The v_{dc} voltage is faster increased by the DC -link control, causing the motor control to go into flux weakening region only over 5600 rpm , once the maximum v_{dc} is reached. Anyway, at higher k_{DCDC} , a larger DC -link voltage margin is imposed, i.e. after the transient, a steady state voltage $v_{dc} = 336\text{ V}$ (120% of $\sqrt{3} |v_{\alpha\beta}^*|$) is required. A larger v_{dc} means the switching losses in the converters are not minimized. On the other side, setting a scalar gain value $k_{DCDC} = 1.1$ guarantees 10% voltage margin, i.e. it converges to a steady-state $v_{dc} = 308\text{ V}$. This means that at medium speed the losses in the converters will be slightly lower if a lower k_{DCDC} is adopted. Therefore, its calibration is a tradeoff between control performance and optimal voltage utilization.

3.2.2 DC/DC control type 2

The trade-off between high control dynamic performance and optimized conversion efficiency is solved in DC -link control type 2 at the cost of calibrating one more parameter, i.e. the scalar gain k_{corr} , and of adding to the control scheme the function $f(FW)$. Based on the FW signal, the safety margin k_{DCDC} is online adapted between the minimum k_{DCDC}^{min} , for optimum voltage utilization, and the maximum k_{DCDC}^{max} , to improve the control dynamic during transients. The effectiveness of the FW signal is highlighted in Figure 3.7, where the simulation depicted was run under the same load cycle of Figure 3.3, with a sharp torque step and acceleration, followed by torque and speed reversals.

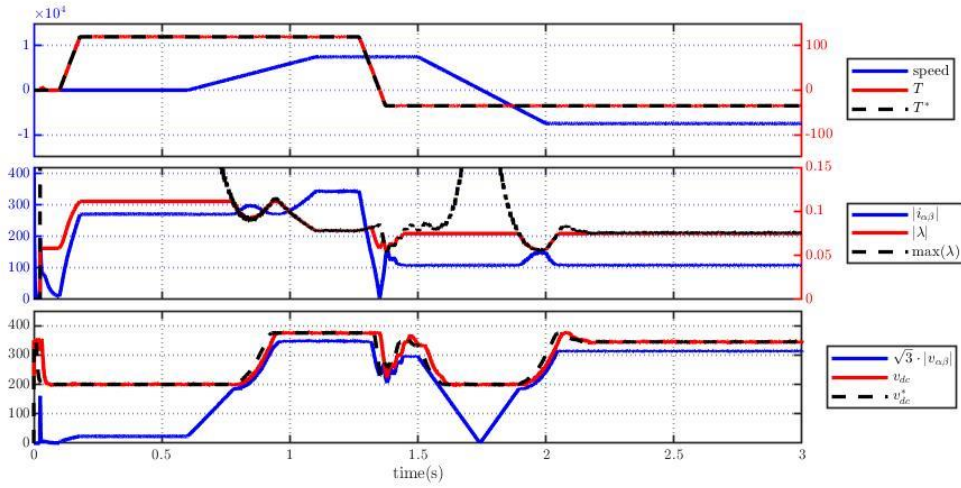


Figure 3. 7: Simulation of the DC/DC control type 2- light flux weakening cycle. Calibration $k_{DCDC} = 1.15$; LPF cut-off frequency = 30 Hz and $k_{corr} = 0.6$.

As can be seen, a low scalar gain value is set, which may the motor control to work under the FW speed range. Indeed, under fast acceleration with a low k_{DCDC} the DC-link control is relatively slow in increasing the voltage v_{dc} , requiring, in extreme conditions, very deep flux weakening. This may lead to significant high current demand and system power losses and eventually inaccurate motor torque control. However, it is avoided by the k_{DCDC} adaptation with the combined action of the v_{dc} feedback and the $f(FW)$ function, ensuring a good dynamic response with the minimum flux weakening request even during sharp transients. Thanks to this approach, it is possible to online adapt the k_{DCDC} based on the actual operating region of the motor, i.e., to increase the scalar gain when the motor is working in FW speed range, leading to a faster variation of the DC-link voltage v_{dc} , and thus limiting the field weakening phenomenon. In other words, it could be said that the DC-link control dynamic of type 2 with a lower k_{DCDC} is pretty similar to the dynamic of type 1 with a higher scalar gain value. Overall, the control becomes more robust and efficient even during sharp speed or torque transients.

Additionally, in most of torque control techniques, a correct current regulation in FW speed range is guaranteed by considering a certain voltage margin, i.e., the v_{dc} is not fully exploited at steady state. If a lower margin is set, it may happen, under certain conditions (e.g., torque reversal in flux weakening speed range), that the DC/DC control becomes ineffective and unable of increasing the reference voltage command v_{dc}^* at higher speed. This means that the motor would steadily works in deep FW under minimum voltage v_{dc} , with significantly low system conversion efficiency. An example of simulation without k_{DCDC} adaptation by the FW signal is depicted in Figure 3.8. As can be noticed, the DC-

link voltage is set by the DC/DC control close to its minimum, even if the motor is running over the base speed. This leads to unnecessary deep flux weakening and high stator current. This can be easily avoided by considering k_{DCDC} regulation under the $f(FW)$ function when the motor operates in the FW region.

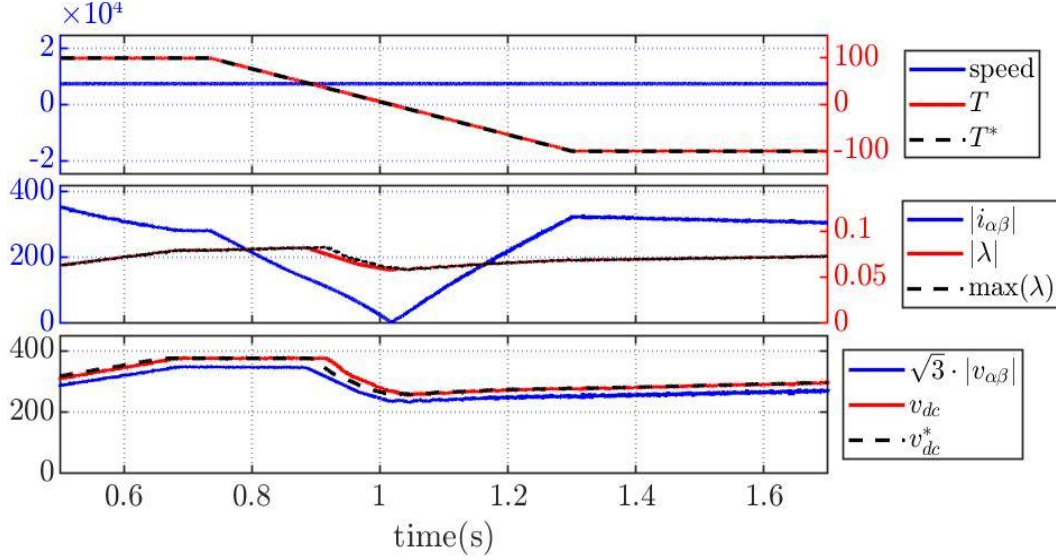


Figure 3. 8: Simulation of the DC/DC control under sharp torque reversal at 7500 rpm (68 Km/h) without k_{DCDC} adaptation.

3.3 DC-link control for a 6-phase Drive

As said, the advantage of the proposed DC -link control algorithm is its implementation whatever the adopted control strategy, since the DC/DC converter and the motor control are treated as independent black boxes. As a consequence, it's possible to develop, debug and calibrate the two algorithms separately, regardless of the choice and calibration of the torque control. Additionally, the independence of the variable DC -link control algorithm from the type or number of phases of the electrical machine, make it suitable for also for multi-three phase drives application. Thus, the DC/DC control was successfully extended to the dual-three phase case, without affecting its high performance. In the six-phase configuration, as said, each three-phase inverter is fed by half of the voltage v_{dc} while the DC/DC converter controls the total DC -link voltage. The balance of the voltage across the two inverter-cell capacitances is guaranteed by the motor control algorithm. As a consequence, only the output voltage of one three-phase inverter unit was input to the DC -link control, and the output of the DC/DC converter was multiplied by a factor 2. A simulation of the variable DC -link control for the six-phase configuration under a complex load cycle is depicted in Figure 3.9, where the motor control strategy under test is now the

CVC-FOC [9].

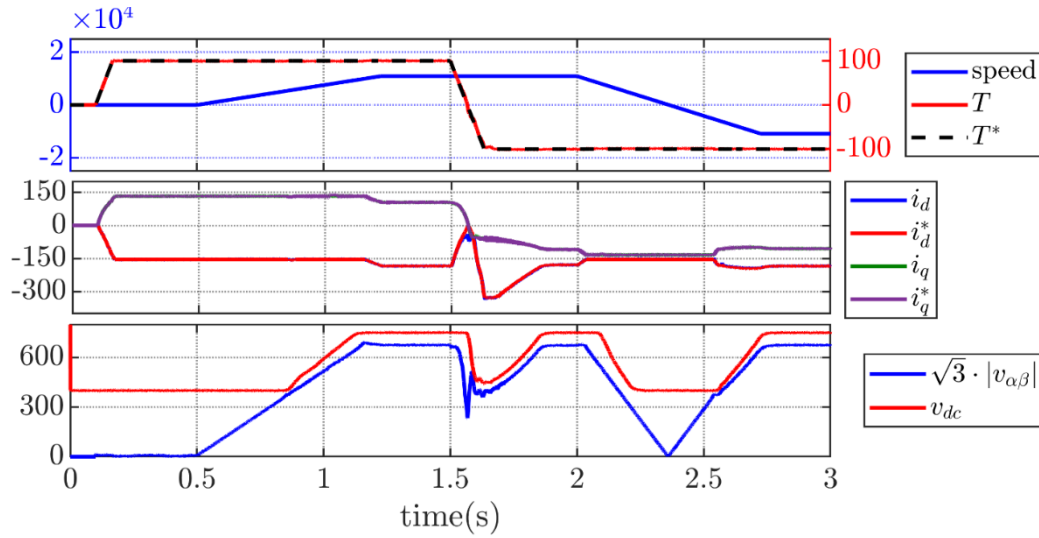


Figure 3. 9: Simulation of the DC/DC control type 2 combined with CVC-FOC torque control for 6-phase configuration: complex load cycle.

As can be noticed, the control works properly as well, with the reference torque accurately tracked. The DC -link voltage is correctly imposed by the DC/DC control. It is increased up to the maximum value (750 V) during acceleration and reduced when the speed decreases, thus reducing the required voltage, and increased again for higher speed in negative direction.

The adopted motor control strategy mainly differs from the DFVC in its slower torque regulation under flux weakening conditions. Consequently, it would be necessary to reduce the feasible bandwidth of the DC/DC control by set the cut-off frequency of the LPF to 10 Hz . The effect of this operation can be easily noted in the larger voltage sag under torque reversal. Anyway, in both the torque control strategies, the variable DC -link voltage does not affect the motor control dynamic. In this way, a regulation of the torque at the best capabilities of the motor control strategy is achieved. Additionally, in order to minimize the power losses, both CVC-FOC and DFVC force the operating point to lay on the MTPA locus, below the base speed ω_b , while at higher speed, field weakening operation is needed, despite the lower efficiency of the drive [9].

3.4 Inverter and DC/DC converter losses analysis

A numerical evaluation of the aggregate losses reduction (DC/DC converter + inverter) based on a loss analysis of the two converters is covered. The losses in the traction inverter and in the DC/DC converter are estimated by considering a standard WLTP

driving cycle for three different types of vehicle, i.e. A-segment vehicle, small SUV and large SUV. Each value of motor torque and speed defined by the WLTP cycle, are converted into current and voltage request by BRUSA. Based on these data and the loss maps, the estimated inverter and DC/DC losses can be computed for each class of vehicle, by selecting the battery voltage and the safety margin values. Figure 3.10 shows an example of losses estimation referred to the test case of an A-segment vehicle. The simulation was run under a battery voltage of 370 V and a safety margin value $k_{DCDC} = 1.1$. The blue curves depict the estimated losses under DC -link variation, whereas the red ones indicate the inverter, DC/DC and the total losses estimation without v_{dc} adaptation.

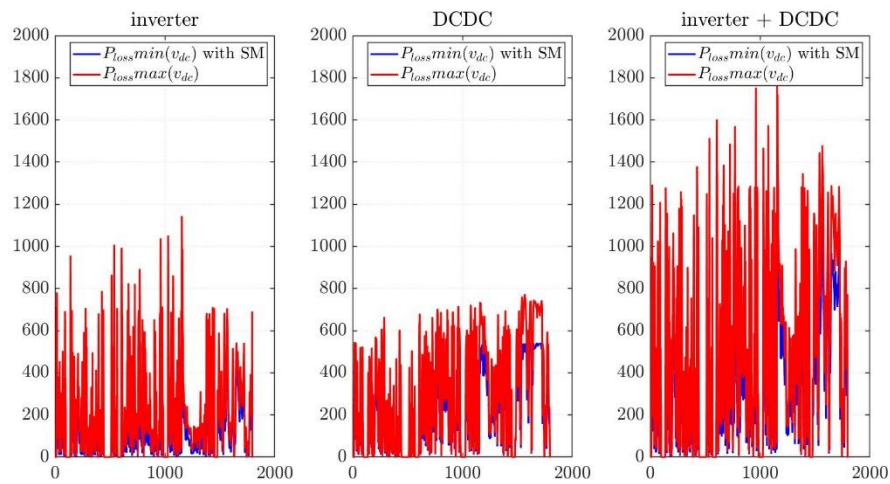


Figure 3. 10: inverter, DC/DC and total losses in the WLTP cycle with $k_{DCDC}=1.1$.

As can be seen, the DC -link voltage adaptation ensures a significant loss reduction in both the traction inverter and the DC/DC converter. Thus, the aggregate losses are strongly minimized thanks to the adopted DC/DC control strategy and, consequently, a significant increase of the conversion efficiency is obtained. This can be easily noticed in Figure 3.11 where the benefit in terms of total efficiency (inverter + DC/DC converter) is evident. Indeed, the figure shows the efficiency of both the converters with and without adapting the DC -link voltage v_{dc} , in the WLTP cycle under test.

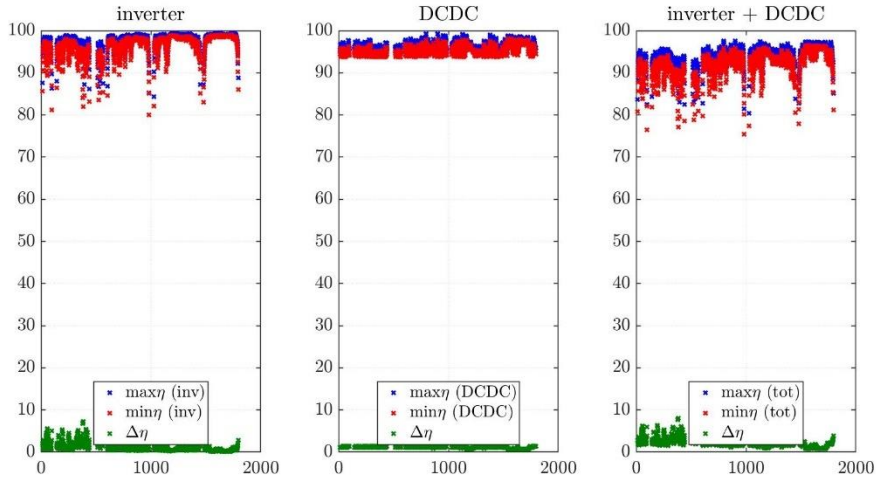


Figure 3. 11: inverter, DC/DC and total efficiency in the WLTP cycle with (blue) or without (red) v_{dc} adaptation.

The average power loss in the inverter and in the DC/DC converter for this test case are reported in Table 5.

	<i>INVERTER LOSSES</i>	<i>DC/DC LOSSES</i>	<i>TOTAL LOSSES</i>
Adapting v_{dc}	176.66 W	349.76 W	590.65 W
Fixed $v_{dc} = 750 V$	240.88 W	258.86 W	453.53 W
Power saving (W)	64.22	90.9	155.12
Power saving (%)	26.66	25.99	26.26

Table 5: Inverter, DC/DC converter and total losses with $k_{DCDC}=1.1$.

Therefore, the benefits in terms of losses reduction referred to this test case can be summarized in a $\approx 27\%$ of power saving in the inverter, 26% in the DC/DC, for a total loss saving of $\approx 26\%$.

The same simulation was run with a safety margin value $k_{DCDC} = 1.2$. Figures 3.12 and 3.13 depict the estimated losses in both DC/DC converter and DC/AC inverter and the correspondent efficiency in the WLTP cycle respectively.

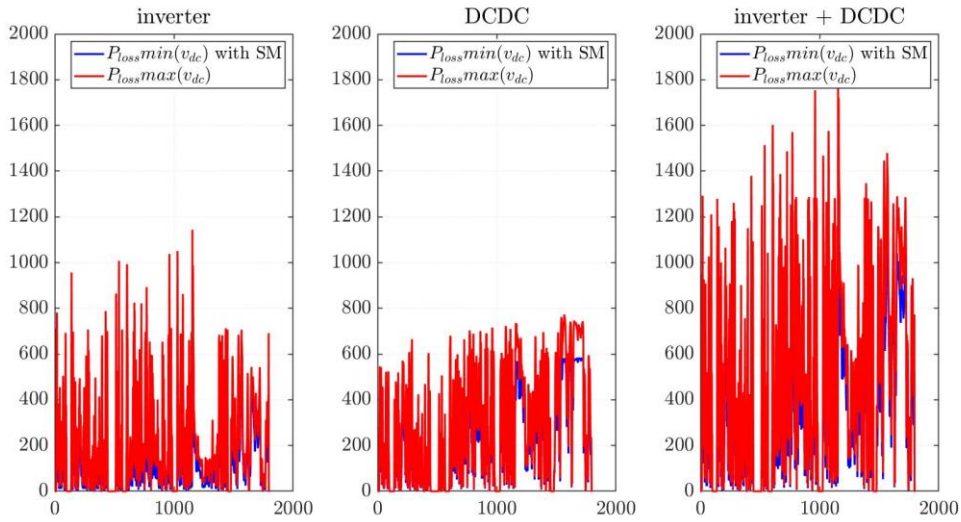


Figure 3. 12: inverter, DC/DC and total losses in the WLTP cycle with $k_{DCDC}=1.2$.

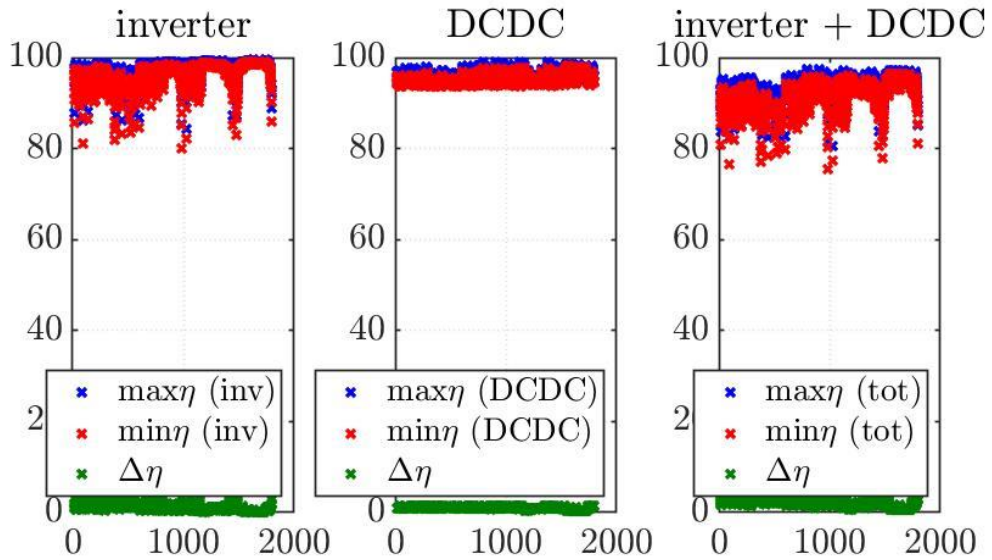


Figure 3. 13: inverter, DC/DC and total efficiency in the WLTP cycle with $k_{DCDC}=1.2$.

The average power loss in the inverter and in the DC/DC converter for this test case are instead reported in Table 6.

	<i>INVERTER LOSSES</i>	<i>DC/DC LOSSES</i>	<i>TOTAL LOSSES</i>
Adapting v_{dc}	240.88 W	349.76 W	590.65 W
Fixed $v_{dc} = 750 V$	170.24 W	265.78 W	444.02 W
Power saving (W)	62.65	83.98	146.62
Power saving (%)	26.01	24.01	24.82

Table 6: Inverter, DC/DC converter and total losses with $k_{DCDC}=1.2$.

As can be noted, the losses are reduced by approximately 26 % in the inverter and 24 % in the *DC/DC*, for a total loss saving of 25 %. Anyway, the losses in the converters are slightly lower if a lower k_{DCDC} is adopted.

3.5 Experimental validation

In this section, experimental results that validate the proposed *DC*-link control strategy are presented. Tests have been carried out by Tecnia research institute, one of the FITGEN partners, in their facilities. The test bench is reported in Figure 3.14, where the traction inverter and motor, the mechanical gearbox, the torque meter and the load machine are included [9].

The FITGEN drive under test is torque controlled, as common for traction applications, while the speed is imposed by the driving machine.



Figure 3. 14: Experimental platform, including the motor under test and the 6-phase inverter [9].

A preliminary set of tests has been carried out to experimentally validate the multiphase torque control combined with the proposed variable DC -link adaptation strategy. The prototype of Figure 3.14 has been used. The nominal parameters of the dual three-phase IPMSM are, once again, the ones summarized in Table I. The following figures depict an example of experimental test where a speed step from 8000 to 13000 rpm has been imposed under constant torque reference. The upper subplot of Figure 3.15 shows the measured current components in dq coordinates for the two 3-phase sets, while the reference currents are depicted in the middle one. The third subplot presents the stator voltage reference, again in dq frame for the two sets. The torque, the imposed mechanical speed and the DC -link voltage adaptation are shown in Figure 3.16.

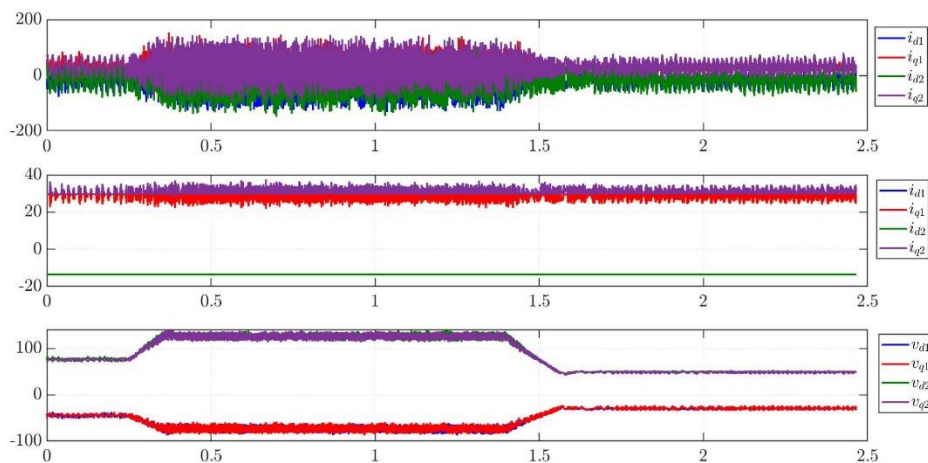


Figure 3. 15: Experimental current and stator voltage vectors in d - q plane.

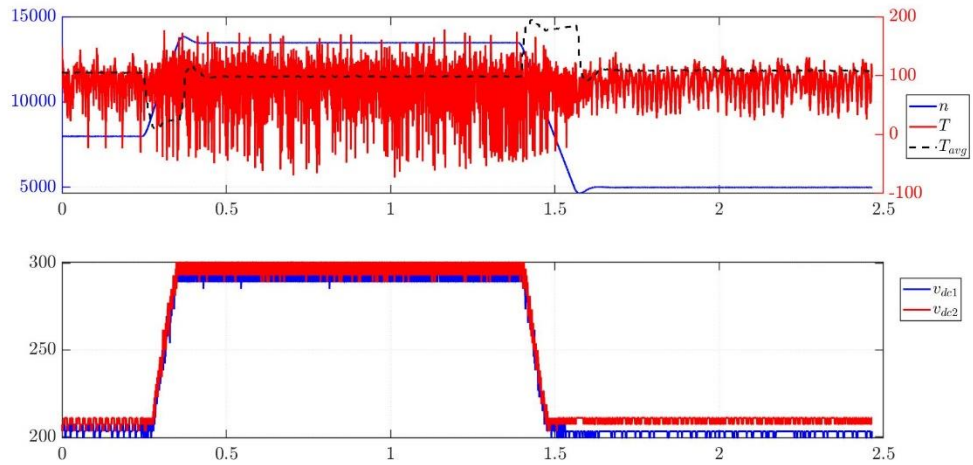


Figure 3.16: Experimental torque trajectory and DC-link voltage regulation under a speed step.

As can be noted, despite the measurement noise and inaccuracies related to the DC/DC converter, the DC -link voltage is correctly imposed by the variable DC -link control, which reacts by increasing the voltage v_{dc} during acceleration. The v_{dc} is instead correctly reduced when the speed decreases.

A second level experimental validations of the proposed technique are currently ongoing in the Austrian Institute of Technology, another FITGEN partner.

CHAPTER 4

4. Conclusions

This work focuses on the evaluation and calibration of an optimized control strategy for online regulating the DC -link voltage in a traction motor drive equipped with a DC/DC converter, for high voltage operation. The DC/DC converter, which feeds the six-phase inverter, aims to boost the battery voltage v_b from a rated 400 V to a controlled DC -link voltage v_{dc} up to 750 V . In particular, the aim of the proposed algorithm is to vary the amplitude of the DC -link depending on the drive operating conditions in order to minimize the power losses in the DC/DC converter and in the traction inverter, without limiting the motor control dynamic performance. This means make it possible to operate in the MTPA region up to the maximum possible speed, avoiding unnecessary field weakening operation, and without limiting the motor control bandwidth. At first, the optimal motor operating point in the dq plane and the correspondent optimal v_{dc} are computed by using the FEM data of the machine, including MTPA tracking and FW operation, both under variable DC -link. Anyway, since these LUTs are computed based on the motor model, the calculated v_{dc}^* setpoint strongly depends on accurate knowledge of its parameters, so it is considered unreliable for practical implementation.

The DC/DC optimal voltage adaptation control comprises two different types, the DC/DC control *type 1* and the DC/DC control *type 2*, able to automatically adapt the optimal v_{dc}^* during operation, without relying on motor data. The first one is characterized by simple implementation and calibration, but requiring a tradeoff between fast motor control dynamic and power saving, i.e. power loss minimization, at medium speed. The DC/DC control *type 2*, instead, gives similar dynamic performance but further optimizes the DC -link voltage v_{dc} when it is between its maximum and minimum value, at cost of more complicated calibration procedure. Particular effort is devoted to the optimal calibration procedure, which focuses on a tradeoff between a fast motor control dynamic with reliable safety margin and power loss minimization. The control *type 1* requires tuning two parameters: the scalar gain k_{DCDC} and the LPF cut-off frequency. The higher k_{DCDC} , the larger safety margin is imposed, permitting a stable torque control under faster motor acceleration, but also the less are the benefits in terms of power losses at medium speed. The LPF avoids unstable or underdamped response, but limits the DC/DC control dynamic. Beside these two parameters, the control *type 2* also requires calibrating the gain

k_{corr} . Moreover, k_{DCDC} is split in two gains k_{DCDC}^{min} and k_{DCDC}^{max} . The DC/DC control is tested when combined with a novel inverter-motor control system, which considers cross-coupling effects in the FITGEN dual-three-phase machine. Therefore, an efficient operation in the whole speed/torque operating range of the motor is expected, including MTPA tracking and FW operation, both under variable DC -link. Furthermore, the algorithm actively balances the input DC -link voltages of the cascaded connected inverter cells.

Moreover, the key advantage of the variable DC -link control is its substantial independence from the motor control algorithm, to be compatible with different types of torque control strategies, e.g., Current Vector Control - Field Oriented Control (CVC-FOC), Direct Torque Control (DTC), Model Predictive Control (MPC) or Direct Flux Vector Control (DFVC). Indeed, the motor control and the DC/DC converter are treated as independent black boxes, permitting to develop, debug and calibrate the two algorithms separately, with large freedom for the choice and calibration of the torque control. The proposed method can be also implemented independently by DC/DC converter structure, which can be integrated with the inverter or not.

To validate the proposed adaptive control, a simulation platform was developed, by considering the FEM data of the electric motor to provide accuracy to the simulation models. Non-linear phenomena like magnetic saturation were also considered. Therefore, the DC/DC control was integrated and thoroughly validated in the Matlab-Simulink environment using accurate modeling of the electrical machine and power electronic converters. The simulation results validate the global control strategy, that is the motor control algorithm + DC/DC control, by its performance. According to the actual operating point, the motor control works correctly, by properly imposing torque and currents while the DC/DC control optimally varies the DC -link voltage.

Lastly, the global control system is implemented in the inverter control unit (dSPACE MicroAutoBox) and validated in an experimental set-up. The experimental test allows a fine-tuning of the control system, considering the physical FITGEN e-axle prototype. Moreover, as said, even if the proposed DC -link control has been developed for a specific EV architecture equipped with a six- phase motor drive, it can be considered an add-on to the torque control algorithm in a wide range of EV applications.

References

- [1] Electric Mobility: Chances and Technical Challenges.
Alois Knoll and Ljubo Mercep and Hauke Stähle. Institute for Robotics and Embedded Systems, Faculty for Informatics, Technische Universität München, Boltzmannstr. 3, 85748 Garching, Germany.
- [2] IEA, “Global EV Outlook 2020,” 2020. [Online]. Available: <https://www.iea.org/reports/global-ev-outlook-2020>. [Accessed June 23rd 2021].
- [3] “European Innovation for Next Generation Electrified Vehicles and Components.”- Eric Armengaud, Omar Hegazy, Bernhard Brandstätter, Valentin Ivanov, Reinhard Tatschl, Michele De Gennaro, Aldo Sorniotti, Joeri Van Mierlo, Christof Schernus.
- [4] “Driving the Future – Electric Mobility a Paradigm Shift & Its Challenges”- Jayadharashini N V, Visteon Technical Services Centre -Chennai , India
- [5] H2020 EU FITGEN D7.4 – “Exploitation Strategy”. Available: https://fitgenproject.eu/files/FITGEN_D7.4_Exploitation%20strategy.pdf.
- [6] “Advanced Functionally Integrated E-Axle for A-Segment Electric Vehicles”- Paolo Pescetto, Mariapia Martino, Gianmario Pellegrino.
- [7] H2020 EU FITGEN D1.3 – “Reliable and scalable design ready for mass manufacturing and dismantling”. Available: https://fitgenproject.eu/files/FITGEN_D1.3_Reliable%20and%20scalable%20design%20ready%20for%20mass%20manufacturing%20and%20dismantling.pdf.
- [8] H2020 EU FITGEN project. Available: <https://fitgen-project.eu/> [Accessed June 23rd 2021].
- [9] “Variable DC-link Control Strategy for Maximum Efficiency of Traction Motor Drives”- Paolo Pescetto, Andres Sierra-Gonzalez, Elena Trancho, Gianmario Pellegrino.
- [10] M. De Gennaro, P. Buechel, A. Primon, O. Bertini, P. Pescetto, J. H. Page, "Interim results of the H2020 project FITGEN: design and integration of an e-axle for the third-generation electric vehicles", 33rd Electric Vehicle Symposium (EVS33) Portland, Oregon, June 14 - 17, 2020.
- [11] H2020 EU FITGEN D2.2 – “Electrical architecture and interfaces”. Available: https://fitgenproject.eu/files/FITGEN_D2.2_Electrical%20architecture%20and%20interfaces.pdf

- [12] “A Flux-Weakening Control Approach for Interior Permanent Magnet Synchronous Motors Based on Z-Source Inverters” - Muyang Li, Student Member, IEEE, Jiangbiao He, Student Member, IEEE, Nabeel A.O. Demerdash, Life-Fellow, IEEE Department of Electrical and Computer Engineering, Marquette University, WI, 53233.
- [13] “A Review on Multiphase Drives for Automotive Traction Applications”- Ahmed Salem, Student Member, IEEE, and Mehdi Narimani, Senior Member, IEEE.
- [14] “Motor loss reduction with high switching frequency SiC inverter,” 2017 IEEE 12th International Conference on Power Electronics and Drive Systems (PEDS), Honolulu, HI, 2017, pp. 754-757-] K. Yamaguchi, K. Katusra and T. Jikumaru.
- [15].
- [16] [https://www.brusa.biz/fileadmin/template/Produkte/Wandler/BRUSA Factsheet BDC546.pdf](https://www.brusa.biz/fileadmin/template/Produkte/Wandler/BRUSA_Factsheet_BDC546.pdf).
- [17] H2020 EU FITGEN D3.1 - “E-axle specification input”. Available: https://fitgen-project.eu/files/FITGEN_D3.1_E-axle%20specification%20input.pdf.
- [18] “Decoupled Vector Control Scheme for Dual Three-Phase Permanent Magnet Synchronous Machines”- Jussi Karttunen, Samuli Kallio, Pasi Peltoniemi, Member, IEEE, Pertti Silventoinen, and Olli Pyrhönen.
- [19] “Control of dual three-phase IPMSM drive with cascaded DC-link capacitors for third generation EV” - Andres Sierra-Gonzalez, Paolo Pescetto, Elena Trancho, Edorta Ibarra, Gianmario Pellegrino, Fernando Alvarez-Gonzalez.
- [20] “Dual Three-Phase Permanent Magnet Synchronous Machine Supplied by Two Independent Voltage Source Inverters”- J. Karttunen, S. Kallio, P. Peltoniemi, P. Silventoinen, and O. Pyrhönen Lappeenranta University of Technology, P.O.Box 20, FI-53851 Lappeenranta, (Finland).
- [21] “PM-Assisted Synchronous Reluctance Machine Flux Weakening Control for EV and HEV Applications” - Elena Trancho, Edorta Ibarra, Antoni Arias, Inigo Kortabarria , Jonathan Ju“rgens, Luca Marengo, Antonio Fricassè, Johannes V. Gragger.
- [22] “IPMSM Torque Control Strategies based on LUTs and VCT feedback for Robust Control under Machine Parameter Variations” - E. Trancho, E. Ibarra, A. Arias, C. Salazar, I. Lopez, A. Diaz de Guerenú, A. Pena-Tecnalia Research and Innovation, Industry and Transport Unit.
- [23] “Variable DC-link voltage powertrain for electrified mobile work machines” -

Christian Pohlandt, Marcus Geimer Institute of Vehicle System Technology, Chair of Mobile Machines Karlsruhe Institute of Technology (KIT) Karlsruhe, Germany.

[24] “A Compact Field Weakening Controller Implementation” - Jonas Ottosson and Mats Alaküla.

[25] “Direct flux vector control of IPM motor drives in the maximum torque per voltage speed range”- G. Pellegrino; E.Armando; P. Guglielmi.

[26] “Sensorless Field Oriented Control of 3-Phase Permanent Magnet Synchronous Motors” – Texas Instruments, Bilal Akin, Manish Bhardwaj, Jon Warriner.